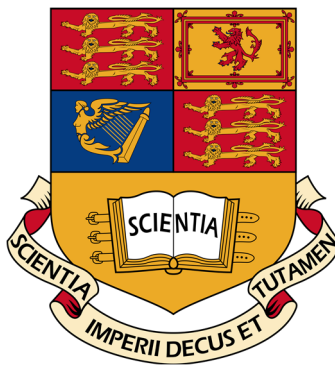


IMPERIAL COLLEGE OF SCIENCE, TECHNOLOGY AND MEDICINE  
DEPARTMENT OF AERONAUTICS

**THE MECHANICAL PROPERTIES AND THE SIZE EFFECT  
OF INDIUM AT ROOM TEMPERATURE**

Dissertation



SERGIU PETRE ILIEV

**Supervisor:** Dr. Vito Tagarielli

**Module:** AE4-406 Individual Project

**Designation:** LRVT01 E/T/A

**Course:** H401

**CID:** 00729069

**Date:** 24.05.2016

Submitted to the Department of Aeronautics on May 24, 2016, in partial fulfillment of the requirements for the degree of Master of Aeronautical Engineering.

Imperial College London  
South Kensington Campus  
London, U.K., SW7 2AZ

## **Preface**

This dissertation contains the manuscript of a paper that shall be submitted for publishing in *Acta Materialia*, Elsevier in May 2016. It is important to note the fact that some data on which the analysis was carried out was determined by the co-authors of the paper. Ms. Xiaorer Chen provided one set of data obtained using the Instron 5969 at room temperature. Mr. Pathan Methab and I jointly obtained compression and instrumented indentation data using the DMTA Analyser. All experiments were replicated independently, reinforcing the results validity. Furthermore, section 6 of the dissertation is not intended for publication. It describes the preliminary testing of indium in liquid nitrogen and represents the starting point of a future study beyond the scope of the current paper.

## **Acknowledgements**

First of all, I would like thank my mentor and supervisor, Dr Vito Tagarielli, for his continuous support and advice throughout my dissertation. The door to his office was always open whenever I encountered difficulties. I am grateful for his knowledge and wise criticism during the analysis phase and for his inexhaustible patience during the experimentation phase of this dissertation. Furthermore, I would also like to thank the following people:

Mr. Roland Hutchins – for 3D printing advice and general workshop guidance.

Mr. Ian James – for help with CNC machining of the PMMA mould.

Mr. Jon Cole – for guidance using the microscopes and fabrication of compression fittings.

Mr. Joseph Meggyesi – for supervision in the DFF laboratory and advice for safe testing.

Mr. Garry Senior – for his supervision working in the composites centre and annealing training.

Mr. Franco Giammaria – for the DAQ and signal acquisition setup as well as LabView training.

Mr. Martin Hervy – for training in using the Microtester.

Dr. Koon-Yang Lee – for granting access to his research lab for micro sample manufacturing.

Mr. Alan Smith – for manufacturing of a foam support for the liquid nitrogen dewar.

Mr. Keith Walker – for providing materials required for testing at cryogenic temperatures

Finally, I must express my very profound gratitude to my parents, little brother and friends for providing me with constant support and encouragement throughout my degree.

This paper was made possible by all these great people.

# Table of Contents

Preface .....	ii
Acknowledgements .....	ii
1. Introduction .....	2
2. Experimental Investigation .....	3
2.1 Material preparation .....	3
2.2 Uniaxial tension.....	4
2.3 Uniaxial compression.....	4
2.4 Three-point bending.....	4
2.5 Vickers indentation experiments .....	5
2.5.1 Vickers micro-hardness tests .....	5
2.5.2 Indentation creep tests .....	5
2.5.3 Instrumented indentation tests .....	5
3. Analytical models.....	6
3.1 Indentation of a power-law creeping material.....	6
3.2 Microbending of a power-law creeping metal.....	8
4. Results & Discussion.....	10
4.1 Uniaxial tension experiment.....	10
4.1.1 Size effect observations.....	10
4.1.2 Linear modulus evaluation .....	11
4.2 Microscope analysis of surface features.....	12
4.3 Uniaxial compression experiment.....	13
4.3.1 Strain rate dependency.....	13
4.3.2 Size effect observations.....	15
4.4 Three-point bending.....	16
4.5 Vickers micro-hardness experiment.....	19
4.6 Constant load indentation (creep) experiment.....	21
4.7 Instrumented indentation experiment .....	24
4.8 Length scale determination .....	26
5. Conclusion.....	29
6. Future improvements: cryogenic temperature experiments.....	30
Annex.....	34

# List of Figures

<b>Figure 1:</b> Dimensions of the dogbone specimens. ....	4
<b>Figure 2:</b> Idealized load vs time history in the hardness experiments, comprising a load ramping phase (I) over a time $t_0$ , followed by a constant load phase (II). ....	5
<b>Figure 3:</b> Schematic of the microbending model showing the plastic hinge .....	8
<b>Figure 4:</b> Tensile response of indium dogbone specimens of various thickness at a target strain rate of $1.7E-03$ . The close grouping of these curves with no segregation between thicknesses indicates there is no size effect. ....	10
<b>Figure 5:</b> The variation of flow stress with thickness at a fixed total strain value of 0.1% (left) and 1% (right). The alignment of the points at the same flow stress level indicates there is no size effect in tension. ....	11
<b>Figure 6:</b> Optical microscope photography of a specimen loaded in tension until the onset of necking. Its features represent incipient shear band formation angled at $\sim 45^\circ$ .....	12
<b>Figure 7:</b> Higher magnification showing in detail the shear bands. The distance between troughs is appears approximately constant across the surface as $\sim 8.34 \mu\text{m}$ . ....	12
<b>Figure 8:</b> True stress-strain variation for the big cylindrical compression specimens tested at three different strain rates with the Instron. Strain rate sensitivity is clearly observed from the three separate curve groups. ....	13
<b>Figure 9:</b> Stress flow at a fixed strain of 5% at a strain rate of $1E-02$ . The data is obtained by testing 20 cylinders of 2 sizes independently with the Instron, DMTA and MT machines. At a strain rate of $1E-02$ . ....	15
<b>Figure 10:</b> Results for all of the three-point bending tests showing the variation of maximum direct stress and strain. All specimens were tested at a nominal strain rate of $1E-03$ . ....	16
<b>Figure 11:</b> Flow stress at a fixed strain value of 0.1% (hallow) and 0.2% (filled) showing there is a size effect since thinner specimens present a higher flow stress at the same strain value. Experiments were carried out with the Instron and DMTA and results are consistent, their average is shown in the present figure. ....	18
<b>Figure 12:</b> Indentation depth versus hardness for Vickers indentation of Indium. Points line-up along lines of constant load for: 10, 24, 50 100, 200, 300, 500, 1000 grams of force. ....	20
<b>Figure 13:</b> Indentation depth versus time history for Vickers indentation of Indium at room temperature, for four values of the applied load. The model (6) has been fitted to each loading case. Data is averaged between three experiments and errors are quantified. ....	21
<b>Figure 14:</b> Hardness versus time history for Vickers indentation of Indium at room temperature, for four values of the applied load. ....	23
<b>Figure 15:</b> Load versus indentation depth for Vickers depth sensing indentation tests carried out with the Instron and DMTA machines. ....	24
<b>Figure 16:</b> Hardness variation with indentation depth for Vickers depth sensing indentation tests carried out with the Instron and DMTA. The model (8) has been fitted to the moving average of the experimental data. ....	25
<b>Figure 17:</b> Fitting of the model to the experimental microbending data. ....	26
<b>Figure 18:</b> Fitting of the model to the experimental depth sensing data. ....	27

**Figure 19:** Extrapolation of the Indium length scale results obtained in this study and the data compiled by Evans and Hutchinson [4] based on the results achieved for Ni [4], Ir [8], Ag [21], Cu [22], and a Superalloy [20]..... 28

**Figure 20:** Comparison of the uniaxial compression response of indium in the non-creep regime (LN<sub>2</sub> temperature, dotted line) and in the creep regime (room temperature, continuous line). 30

**Figure 21:** Comparison between the depth sensing response of indium in the non-creep regime and in the creep regime ..... 31

**Figure 23:** Comparison of the average experimental data in the creep and non-creep regimes. The analytical model has been fitted to the room temperature data..... 31

**Figure 22:** Hardness variation with depth for the non-creep regime (LN<sub>2</sub> temperature, blue dotted line) compared to that in the creep regime (room temperature, black continuous line). 31

## List of Tables

**Table 1:** Numerical values of the creep exponent  $N$  and the constant  $C_\sigma$  determined via power-law fitting of experimental data represented as log-log flow stress vs. strain rate (Annex D). These experiments were carried out with the Instron, DMTA and MT machines on compression specimens of two different nominal dimensions. .... 14

**Table 2:** Numerical values of the creep exponent  $N$  and the constant  $C_H C_\sigma$  determined via least-square fitting of (6) to the experimentally determined indentation depth vs. time histories in Fig. 13, for  $t_0 = 2s$  and  $C_A = 24.5$ ..... 21

## List of Abbreviations

DFF	= Dynamic Fracture and Forming Laboratory at Imperial College London
DMTA	= Dynamic-Mechanical Thermal Analysis (DTMA) RSA-G2 machine, 35 N load cell
FCC	= Face Centred Cubic crystal structure
GND	= Geometrically Necessary Dislocations
HPI	= High Purity Indium
Instron	= 5960 Dual Column Mechanical Testing System, 10 N and 100 N load cell
MT	= Microtester system for tensile and compression tests, 200 N load cell
PMMA	= PolyMethylMethAcrylate, a transparent thermoplastic material
SSD	= Statistically Stored Dislocations

# The mechanical response of high-purity Indium

S. P. Iliev, C. Xiaoer, M. Pathan, and V. L. Tagarielli\*

*Imperial College London, Aeronautics Department, South Kensington, London, SW7 2AZ, UK*

## Abstract

Tension, compression, bending and indentation experiments are conducted on high purity Indium at room temperature and low strain rates. The material displays a ductile viscoplastic response, found to be size-independent in tension and compression. A size effect is detected in bending and indentation, associated to a length-scale of order 50-100  $\mu\text{m}$ . Simple analytical models are built to aid interpretation of the test results.

**Keywords:** Indium, size effect, creep, indentation, bending, compression, tension, length scale

**Paper shall be submitted to Acta Materialia, May 2016**

# 1. Introduction

There are few studies focusing on the mechanical properties of Indium, because it is a metal with low specific strength and modulus of elasticity and unsuitable for structural applications. However, unlike most pure metals, which reach the creep regime at temperatures over 1000°C, Indium has a very low melting point of just 156.61°C. Therefore, at room temperature (22°C) it is at a homologous temperature of 0.69 and deforms by power law creep. This makes it ideal for studying creep phenomena. Furthermore Indium has vast applications in electronics industry. In the aerospace field, Indium is used as a propeller in Field Emission Electric Propulsion Microthrusters. Recently it was a strong contender for use in the E.S.A. Pathfinder mission [1]. Therefore it is important to characterize its mechanical properties and size effect.

Ashby [2] has proposed that geometrically necessary dislocations associated with gradients of plastic strain enhance material strength and lead to size effects in the micron range. This has led to a large number of investigations into size effects in plasticity. For example, an increased yield strength with decreasing specimen size has been observed in microtorsion by Fleck *et al.* [3] and in microbending experiments [4], [5]. Likewise, an increase in hardness with decreasing indentation depth has been observed by several authors including: Stelmashenko *et al.* [6], McElhaney *et al.* [7], Poole *et al.* [8] and Swadener *et al.* [9]. These investigations focused on metals at room temperature, displaying an approximately rate-independent response; no similar investigations were done on metals in the creep regime. This paper explores the size dependence of the mechanical response of this material in the creep regime.

Strain gradient plasticity theories have been developed by several authors to account for the observed size effects (e.g. [10], [11], [12], [13]). These theories contain one or more material length scales and typically predict a strength elevation when the specimen size is comparable with the material length scale. Recently, Evans and Hutchinson [5] have shown that the material length scale increases with the diminishing yield strain of the material. Annealed indium has a particularly low yield strain of  $1.5 \times 10^{-4}$  which suggests a material length scale of the order of tens of microns. This is significantly larger than that of materials previously tested, and would allow for an easy measurement of size effects at a relatively large scale.

Indium is difficult to test and process to obtain a smooth surface finish, therefore experimental studies on this material are scarce. Weertman [14] conducted constant load tensile tests on indium wires at room temperature, and observed a creep exponent of  $N \cong 0.2$ . Lucas and Oliver [15] performed instrumented indentation on indium with a Berkovic indenter, determining a creep stress exponent of  $N \cong 0.2$ . Galli and Oyen [16] conducted room temperature indentation tests with a spherical indenter to a maximum depth on the order of 10  $\mu\text{m}$  and determined values for the creep exponent between 0.1 and 0.2.

This study presents the results of uniaxial compression, tension, bending and indentation tests on high-purity Indium, exploring the dependence of the response upon strain rate and specimen size. The paper is organized as follows. Details of the experimental methods used are provided in section 0. To aid interpretation of test results, simple analytical models are constructed in section 3. Results are presented and discussed in section 4. The paper concludes with section 5.

## 2. Experimental Investigation

### 2.1 Material preparation

All specimens were manufactured from a high-purity (99.999%) Indium ingot with initial grain size of order 0.5 mm. The material was dense but soft and the ingot could be cut, with a heavy duty knife, in small pieces. Such pieces were slowly hot-pressed, at a temperature of 60 °C, between two microscope glass slides, to obtain flat indium plates of smooth surface finish and thickness of a few millimeters. These plates served as indentation specimens and as a base material for production of the other specimen types. In preliminary experiments, with the help of accompanying microhardness tests, it was found that such large plastic deformation hardened the material substantially. An annealing procedure was developed by trial and error in order to restore the material hardness to its original value; this included gradual heating from room temperature to 80 °C in 30 min, holding this temperature for 4 hours, then cooling to room temperature (22 °C) in 1 hour.

Specimens for compression tests were produced starting from Indium plates of thickness 10 mm and 5 mm. Two circular punches with diameters 6 mm and 3 mm were used to extract rods from the plates. Subsequently, these cylinders were slowly pressed into a nylon mould by hand, removing excess material with a razor to obtain a flushed surface with the mould. This process restored the circular shape of the specimens and ensure flat and parallel faces. After this manufacturing step, the annealing procedure described above was repeated prior to testing

Specimens for tension and bending required thinner HPI plates. These were manufactured by hot rolling (80 °C) the 5 mm Indium plates in an Imperia pasta machine with polished and adjustable stainless steel rolls, allowing production of indium sheets of thickness in the range 0.25 – 2 mm. Rectangular specimens for bending tests were cut with a razor from Indium sheets of different thicknesses. Dogbone shaped specimens were used in the tension tests (dimensions presented in Fig. 1). These were extracted from the Indium sheets with a Zwick/Roell ZCP punch. Bending and tension specimens were annealed prior to testing.

Annex A presents the testing machines used to carry out the experiments and Annex B contains the technical drawings of parts custom built to support the manufacturing and experimentation stages.

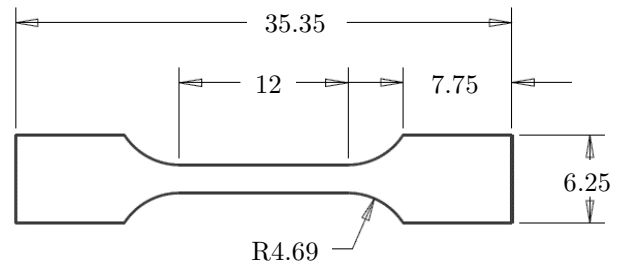


**Figure 1:** Dimensions of the dogbone specimens.  
(all in mm)

## 2.2 Uniaxial tension

Tensile tests were conducted with a micro-tester of 200 N capacity. The specimens were gripped by flat steel plates and forced to elongate, while the tensile force was measured by a resistive load cell. Two reflective strips were glued in the gauge portion of the dogbone specimen to measure strain via a laser extensometer. All tests were conducted at a nominal strain rate of  $1.7 \times 10^{-4} \text{ s}^{-1}$ .

## 2.3 Uniaxial compression

Circular cylinders of diameter 3.5 and 8 mm were tested in compression using both an Instron 5969 machine, the micro-tester described above and a DMTA analyzer (TA Instruments, RSA-G2). Strain was measured via a video extensometer and a laser extensometer tracking, both tracking the position of the loading platens as well as a linear variable differential transformer in the case of the DMTA. Tests were conducted at nominal strain rates of  $10^{-1}$ ,  $10^{-2}$  and  $10^{-3} \text{ s}^{-1}$ .

## 2.4 Three-point bending

A bespoke three-point bending fixture was designed and 3D printed in ABS plastic; this simply consisted of two rollers of radius 1 mm at a span of 20 mm, and of a loading roller of the same radius. These were connected to an Instron tensometer by mechanical fastening and were used to load in bending beams of Indium with thicknesses ranging from 0.25 to 2 mm. The bending force was measured by a resistive load cell of capacity 10 N, the deflection was measured via a laser extensometer of resolution 1 micron. Beams of different thickness were tested and force versus deflection histories were recorded. The rate of deflection was chosen as  $\dot{\delta} = \dot{\epsilon}_{max} L^2 / 6t$  such to guarantee an equal maximum elastic strain rate  $\dot{\epsilon}_{max} = 10^{-3} \text{ s}^{-1}$  for all beam thicknesses.

## 2.5 Vickers indentation experiments

Three different types of Vickers indentation tests were performed in this study, as detailed below.

### 2.5.1 Vickers micro-hardness tests

A Tukon 1202 Micro-Hardness Tester with a Vickers indenter was employed to measure hardness at loads in the range 98.1 mN to 19.61 N. This machine operates by progressively releasing a dead weight over the sample, via a mechanism, and then holding the load constant for a prescribed amount of time, before it is removed. Preliminary measurements showed that the load ramping phase, for the case of indium specimens, lasts approximately  $t_0=2\text{s}$  and occurs at an approximately constant load rate  $\dot{P}$ , i.e.  $P_0 = \dot{P}t$ . The loading history associated with this experiment is sketched in Fig. 2. The duration of the dwell phase was chosen as 5 s, giving a total time  $t_1 = 7\text{s}$ .

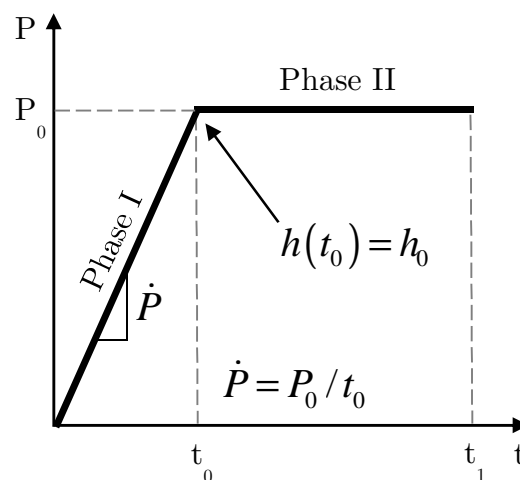


**Figure 2:** Idealized load vs time history in the hardness experiments, comprising a load ramping phase (I) over a time  $t_0$ , followed by a constant load phase (II).

Upon removal of the load, the indentation footprint was observed via an optical microscope; this was fairly square and regular at all loads. Image analysis was used to measure the projected area of indentation to determine the hardness  $H$ . In a second set of measurements, the contact area was determined from measurements of the indentation diagonals. As presented in section 4.5, the difference between the two methods was found to be small. Thus hardness values obtained from measurements of the indentation diagonals are used in the following sections.

### 2.5.2 Indentation creep tests

The experimental setup described in section 2.5.1 was also used to conduct additional microhardness experiments at loads in the range 0.245 N to 1.962 N. For each value of the load, indentation experiments were repeated several times (at different locations) on the sample surface, holding the load for a time ranging from  $t_1 = 10\text{ s}$  to  $t_1 = 1000\text{ s}$ .

### 2.5.3 Instrumented indentation tests

Instrumented indentation was performed using both an Instron tensometer (Instron 5969) and a DMTA analyzer (TA Instruments, RSA-G2) at room temperature. A Vickers indentation tip was displaced, at a constant rate, against a stationary, flat 5 mm thick Indium sample, whilst accurately recording the indentation force (with a resolution of 10 mN for the Instron and 0.1 mN for the DMTA) and the indenter displacement (with a resolution of 300 nm for the Instron and 1 nm for the DMTA) at a frequency of 100 Hz. The indentation speed was chosen as  $7.5\text{E-}03\text{ mm/s}$ .

### 3. Analytical models

This section presents the construction of simple analytical models to aid with the interpretation of experimental results, particularly with respect to size-dependence of strength. The models assume that the material is creeping and its response is size-independent. Thus a comparison to the experimental data can highlight the measured size dependence of the response. Additionally, two analytical models have been developed to calculate the length scale and yield stress of indium from microbending and indentation data. These are presented in Annex C.

#### 3.1 Indentation of a power-law creeping material

The following model helps analyse the microhardness measurements presented in sections 4.5, 4.6 and 4.7. It characterises the indentation of a power law creeping solid, absent any material size effects, when subjected to the load history sketched in Fig. 2.

The average plastic strain rate under the indenter is proportional to  $\dot{h}/h$  since  $\dot{\epsilon} = C_\epsilon \dot{h}/h$  [17], [18], where  $C_\epsilon$  is a material property,  $h$  is the indentation depth and the dot denotes differentiation with respect to time.

The uniaxial stress in the solid  $\sigma$  depends upon the axial strain rate via:

$$\sigma = \sigma_0 \left( \frac{\dot{\epsilon}}{\dot{\epsilon}_0} \right)^N = C_\sigma \dot{\epsilon}^N \quad (1)$$

where  $C_\sigma$  and  $N$  are material constants for a given temperature. There are to be determined experimentally (Table 1, section 4.3.1). The material hardness  $H$  is defined as the average pressure under the indenter, proportional to the flow stress via:

$$H = C_H \sigma \quad (2)$$

where  $C_H$  is approximately 3 (Tabor factor [19]). The true contact area is assumed to scale quadratically with indentation depth  $h$  according to the geometric relation:

$$A = C_A h^2 \quad (3)$$

This assumption neglects any pile-up or sink-in effects, which were negligible in the indentation tests performed, as presented in section 4.5. For a Vickers indenter it is  $C_A = 24.5 \text{ MPa s}^N$

Following the load history presented in Fig. 2, in the first phase, the load is ramped according to  $P = t(P_0/t_0)$ . Combining this with the definition of hardness, (1), (2) and (3) one obtains:

$$H(h, \dot{h}) = \frac{P}{C_A h^2} = C_H C_\sigma \left( \frac{\dot{h}}{h} \right)^N \quad (4)$$

Then the indentation depth can be modelled by:

$$h(t) = K_R t^{(N+1)/2} \quad \text{where} \quad K_R = \sqrt{\frac{P_0}{C_H C_\sigma C_A t_0}} \left(\frac{2}{N+1}\right)^{\frac{N}{2}} = \text{constant} \quad (5)$$

for the ramping phase of the load history in Fig. 2. When  $t > t_0$  the load  $P = P_0$  and is kept constant at this maximum value. Substituting  $P = P_0$  in (4) and integrating with the initial condition  $h_0 = h(t_0)$ , one obtains the following expression for the variation of  $h$  with time:

$$h(t) = \sqrt{\frac{P_0}{C_H C_\sigma C_A}} \left\{ \frac{2t[(N+1)] - t_0}{N(N+1)} \right\}^{\frac{N}{2}} \quad (6)$$

Through differentiation and substitution it is possible to obtain expressions of hardness variation:

$$H(t) = C_H C_\sigma N^N \left[ N t_0^{\frac{N^2+N-2}{2N}} + 2(t-t_0) \right]^{-N} \quad (7)$$

Therefore hardness does not depend on load, even accounting for the time-dependent behaviour of the material, this is because the indenter is self-similar. Finally, the hardness can be written in terms of the penetration depth  $h$  and speed  $\dot{h}$ :

$$H(h, \dot{h}) = K_D \dot{h}^N h^{-N} \quad \text{where} \quad K_D = C_H C_\sigma C_\varepsilon^N = \text{constant} \quad (8)$$

The indenter penetration speed  $\dot{h}$  is kept constant throughout the experiment. Therefore, the hardness  $H$  can be simply calculated from the recorded displacement data,  $h$ .

### 3.2 Microbending of a power-law creeping metal

An analytical model shall be developed for to model the maximum stress and strain obtained in the three-point microbending experiment (section 4.4). Since Indium is in the creep regime at room temperature, its response is assumed to follow a power-law and size effects are not accounted for. The Indium beams are assumed to be rigidly plastic with yield stress  $\sigma_y$ . They progressively collapse by forming a plastic hinge in a small region of width equal to the thickness of the beam  $t$ , centred at the mid-span. This ‘plastic-hinge’ model is presented in Figure 3.

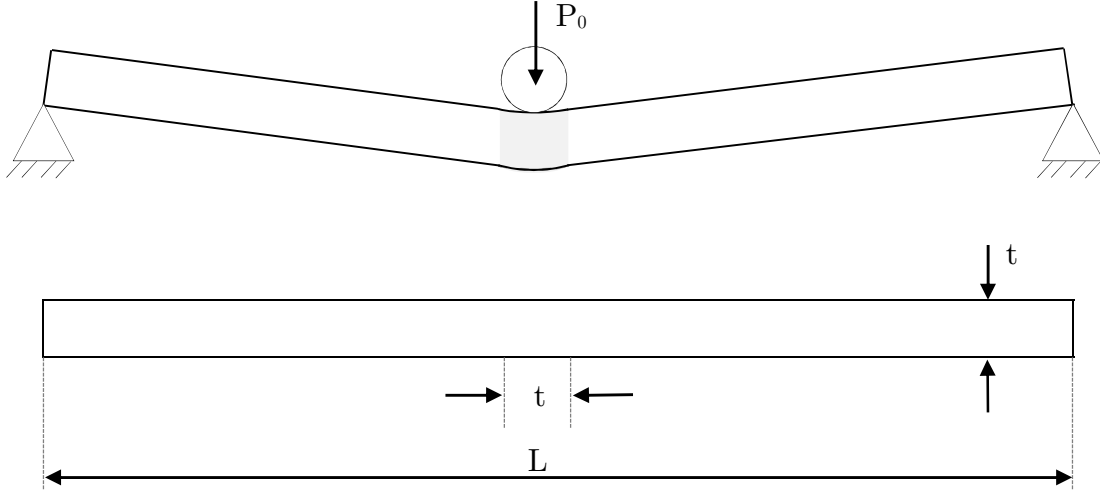


**Figure 3:** Schematic of the microbending model showing the plastic hinge (small zone of localized plastic deformation at mid-span) as well as the straight and rigid regions.

Within the plastic hinge the strain contribution to the yield stress expression is assumed to be insignificant compared to that of the strain rate. Thus the expression of the yield stress can be simplified to the following function:

$$\sigma_y = \sigma_0 + A|\dot{\epsilon}_{(z)}|^N \quad (9)$$

The model assumes the material has the same strain rate dependency in tension and compression:

$$|\dot{\epsilon}_{(z)}|^N = \begin{cases} -(-\dot{k}z)^N & \text{for } z \in [-h/2, 0] \\ \dot{k}z & \text{for } z \in (0, h/2) \end{cases} \quad (10)$$

where  $\dot{k}$  is the curvature rate of the plastic hinge and  $z$  is the through thickness coordinate starting from the centreline and running perpendicular to it in the direction opposite to the load. Now the moment can be found by integrating the stress distribution through the thickness from equations (9) and (10).

$$M = 2b \int_0^{t/2} [\sigma_0 + A(\dot{k}z)^N] z dz \quad (11)$$

where  $b$  is the width of the beam. Solving the integral yields:

$$M = \frac{bt^2}{4} \sigma_0 + \frac{bt^{N+2}}{2^{N+1}(N+2)} A \dot{k}^N \quad (12)$$

For simplicity, it is possible to assume small angle since the deflection imposed during the experiments was small compared to the length of the beams ( $\delta \ll L$ ). Then a relation between the force and the moment is provided by conservation of energy:

$$F\delta = 2M \frac{\delta}{L/2} \leftrightarrow F = \frac{4}{L} M \quad (13)$$

Using (12), the force can be expressing as a function of the curvature rate:

$$F = \frac{bt^2}{L} \sigma_0 + \frac{bt^{N+2}}{2^{N-1}(N+2)L} A \dot{k}^N \quad (14)$$

The curvature of the plastic hinge can be obtained from geometric considerations and expressed as a function of the mid-span deflection  $\delta(t)$ :

$$k = \frac{4L}{t} \frac{\delta}{L^2 + 4\delta^2} \quad (15)$$

Then, differentiation with respect to time gives the curvature rate as:

$$\dot{k} = \frac{4L}{t} \frac{L^2 - 4\delta^2}{(L^2 + 4\delta^2)^2} \dot{\delta} \quad (16)$$

Where  $\dot{\delta}$  is the velocity of the test head  $\dot{\delta} = v = \frac{\dot{\varepsilon}_{max} L^2}{6t}$ , as described in 2.4,  $\dot{\varepsilon}_{max} = 10^{-3} \text{ s}^{-1}$ . Assuming Euler-Bernoulli beam theory applies, the stress at the mid-span lower surface is a function of the force  $\sigma_{max} = \frac{3L}{2bt^2} F$ . This can be expressed in terms of  $\varepsilon_{max}$  by combining (14) and (16). Finally, the equation of the model simplifies to:

$$\sigma_{max} = \frac{3}{2} \sigma_0 + \frac{3^{1-N}}{N+2} A \left\{ \frac{\dot{\varepsilon}_{max} L}{t} \frac{1 - 4(L\varepsilon_{max}/6t)}{[1 + 4(L\varepsilon_{max}/6t)^2]^2} \right\}^N \quad (17)$$

The maximum strain at the mid-span lower surface can be obtained from  $\varepsilon_{(z)} = kz$  and (15) as:

$$\varepsilon_{max} = \frac{2L\delta}{L^2 + 4\delta^2} \quad (18)$$

## 4. Results & Discussion

### 4.1 Uniaxial tension experiment

#### 4.1.1 Size effect observations

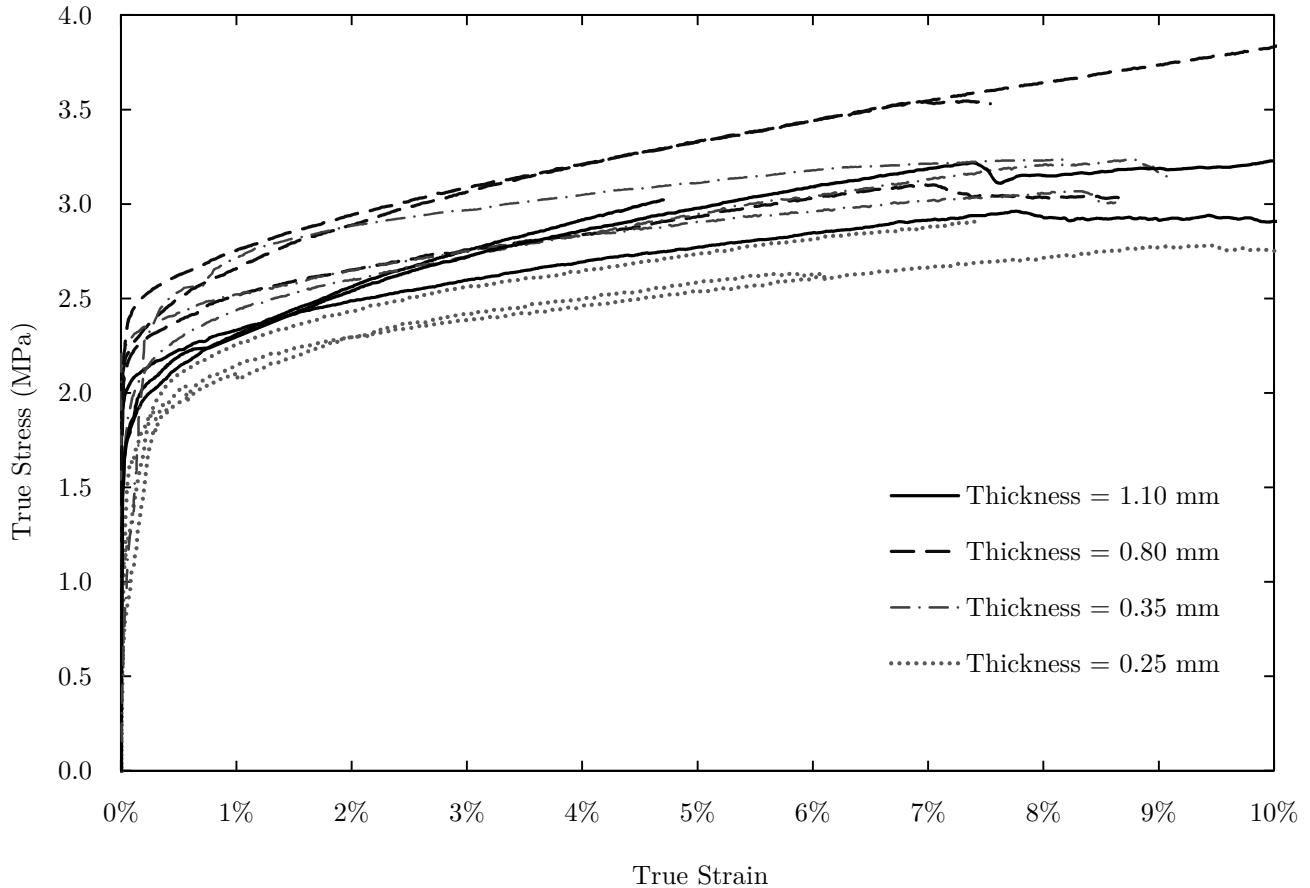


**Figure 4:** Tensile response of indium dogbone specimens of various thickness at a target strain rate of  $1.7E-03$ . The close grouping of these curves with no segregation between thicknesses indicates there is no size effect.

In uniaxial tension there is no strain gradient, such that the strain is constant with respect to the thickness coordinate. Therefore it is expected that there are no effects associated with strain gradient plasticity that would strengthen the material.

The true stress vs. strain curves presented in Fig. 4 do not show significant variation from the thin (0.25 mm) to the thick samples (1.1 mm). This indeed supports the hypothesis that there is no size effect in tension.

To reinforce this point, it is possible to focus at the material response to very small strains. Observing Fig. 5 it becomes clear that the thin samples do not exhibit a larger flow stress and thus are of the same strength as those that are thicker.

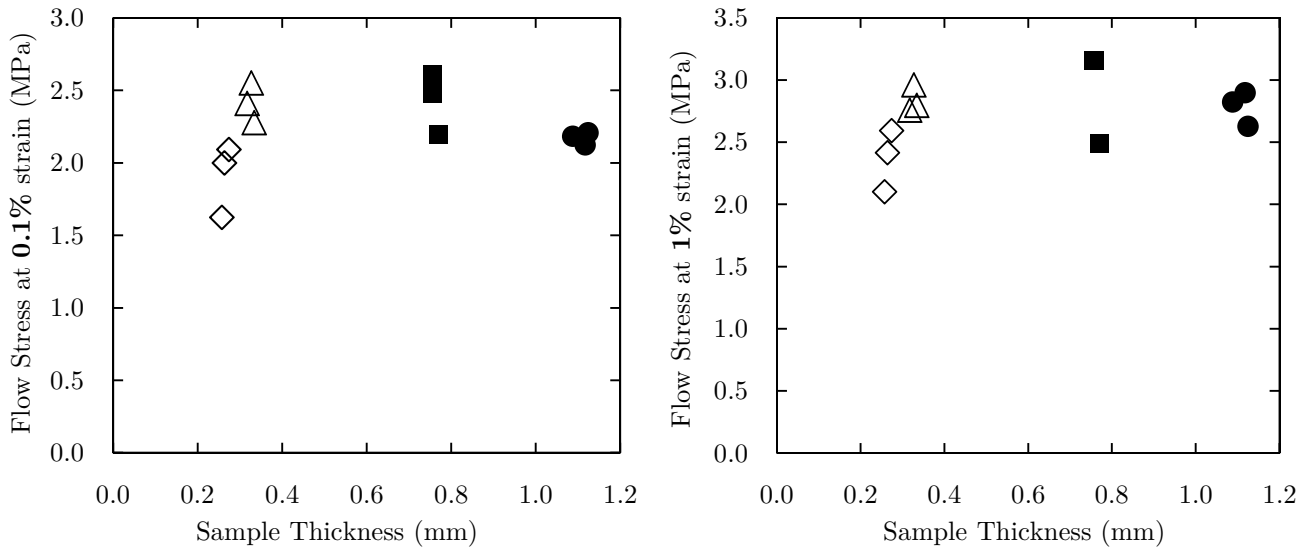


**Figure 5:** The variation of flow stress with thickness at a fixed total strain value of 0.1% (left) and 1% (right). The alignment of the points at the same flow stress level indicates there is no size effect in tension.

Moreover, the same material behavior is observed at a fixed strain of 0.1% and 1%. The flow stress increases by approximately 20% between these two fixed strains, however this happens across samples of different thicknesses. Finally, the fact that, within error bounds, the flow stress in Fig. 5 is the same at multiple thicknesses (i.e. points are horizontally aligned) indicates there are no size effects in tension.

#### 4.1.2 Linear modulus evaluation

The elastic portion of stress-strain curve is very small for Indium at room temperature since the material yields at approximately  $1.5 \times 10^{-4}$  strain. This makes it challenging to evaluate the Young Modulus by focusing on the slope of the stress-strain curves in the initial linearly-elastic region. However, this was accomplished by using a high data acquisition rate and a small strain rate.

Using a linear fit through the elastic region ( $\sigma < 1 \text{ MPa}$ ) of the stress-strain curves from Fig. 4, the Young modulus was determined as 12.03 GPa. This result has a scattered of 9% and is consistent with established results, being within 5.6% from the value of 12.74 GPa established by ASM International [20] for Indium in tension at 20°C.

## 4.2 Microscope analysis of surface features

After etching in a 10% volume solution of hydrochloric acid, optical microscopy revealed a mean grain size of  $500\ \mu\text{m}$ . An atomic force microscope in non-contact mode was used to analyze the surface roughness of the hardness samples measuring a RMS peak-to-valley roughness of  $35\ \text{nm}$ .

Dogbone specimens tested until various levels of strain revealed, under the optical microscope, the surface features reproduced in Fig. 6 and 7. Upon comparison it became clear that both the number and depth of shear bands increase as the sample is subjected to higher tensile loads. Analyzing Fig. 7, it is possible to determine the shear band spacing by counting the pixels between troughs as  $\sim 95\ \text{px}$  which equates to a distance of  $\sim 8.34\ \mu\text{m}$ .

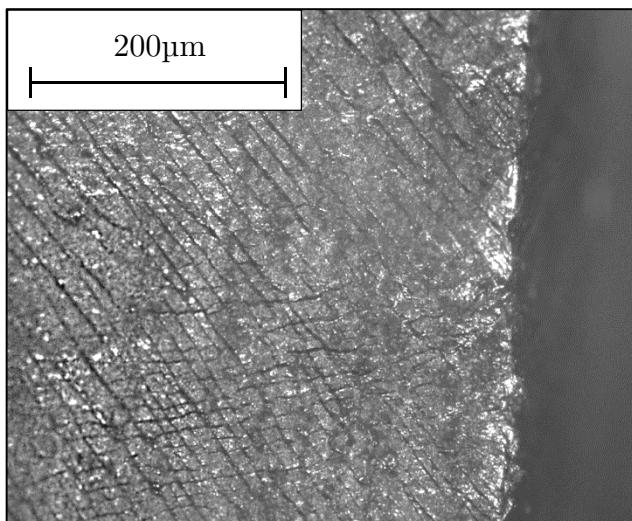


**Figure 6:** Optical microscope photography of a specimen loaded in tension until the onset of necking. Its features represent incipient shear band formation angled at  $\sim 45^\circ$  from the direction of the applied load.

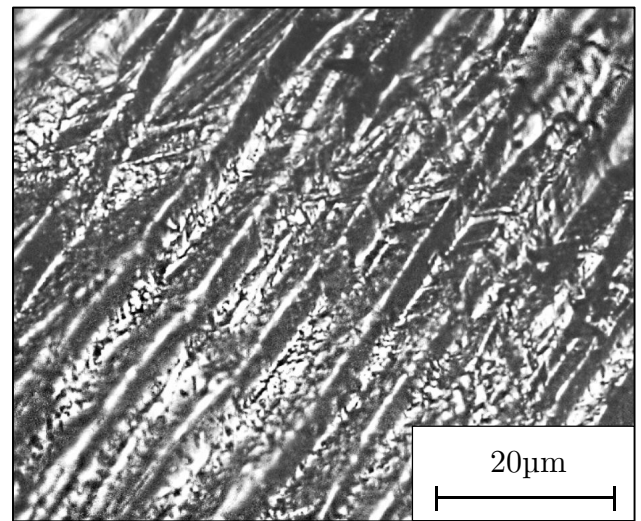


**Figure 7:** Higher magnification showing in detail the shear bands. The distance between troughs is appears approximately constant across the surface as  $\sim 8.34\ \mu\text{m}$ .

### 4.3 Uniaxial compression experiment

#### 4.3.1 Strain rate dependency

The measured compressive response is shown in Fig. 8 for three values of nominal strain rate:  $10^{-3}$ ,  $10^{-2}$  and  $10^{-1} \text{ s}^{-1}$ . Due to the fact that the cross-sectional area and height of the specimens continuously varied throughout the experiments, the true stress and strains are presented for analysis instead of the nominal values.

At room temperature, primary creep occurs up to an axial strain of order 0.1 followed by secondary, power law creep, such that the stress depends upon strain rate but not strain. This is confirmed by the grouping of the true stress-strain curves. The material consistently has a stronger response when subjected to high strain rates.

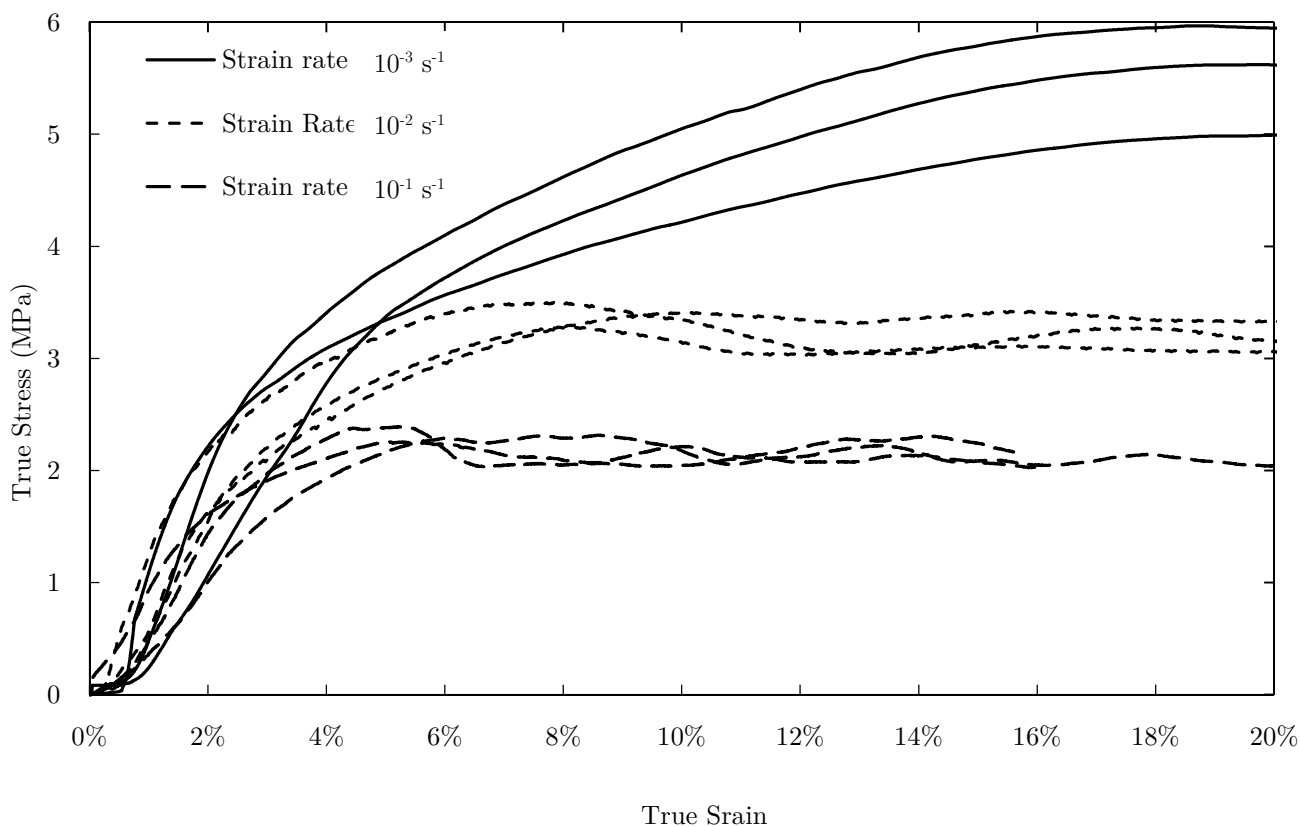


**Figure 8:** True stress-strain variation for the big cylindrical compression specimens tested at three different strain rates with the Instron. Strain rate sensitivity is clearly observed from the three separate curve groups.

The stress-strain gradient increases significantly from approximately 80 MPa (at  $\dot{\epsilon} = 10^{-3} \text{ s}^{-1}$ ) to 110 MPa (at  $\dot{\epsilon} = 10^{-1} \text{ s}^{-1}$ ) this would suggest a stiffening associated with an increase in strain rate. However the values of the initial slope are not feasible as they are two orders of magnitude below the expected value of 12.74 GPa [20] and those already determined in section 4.1.2. This is due to the limitations of the machines use. Even the most precise displacement measurement method used (in the DMTA experiments) had resolution of 1  $\mu\text{m}$ . Since the specimens yield at strain values of the order of  $10^{-4}$ , for cylinders 7.2 mm tall, the linear-elastic region ends is just within

the 1<sup>st</sup>  $\mu\text{m}$  of displacement. This makes it impossible to capture the initial portion with the equipment used. Also, the surfaces of the cylinders are not perfectly parallel and within 1  $\mu\text{m}$  of height difference across the diameter. This is due to precision limitations in manufacturing. Therefore, the initial 1% strain region shall not be considered for the purpose of this analysis.

Looking at Fig. 8 it can be observed that the true stress reaches a steady state ‘plateau’ at a certain strain value:  $\sim 5\%$  for the  $10^{-1} \text{ s}^{-1}$  curve,  $\sim 8\%$  for the  $10^{-2} \text{ s}^{-1}$  curve, respectively  $\sim 18\%$  for the  $10^{-3} \text{ s}^{-1}$  curve. This phenomenon can be explained by the continuous hardening of the since the GND and SSD density increases. This process occurs until a saturation point is reached where the dislocation density remains relatively constant. A higher strain rate is associated with a higher rate of dislocation density growth, which in turn makes the material reach a saturation phase at a lower strain value.

In order to further quantify strain rate effects, and analyze if they correspond to a power-law creep model, data from three different experiments, using the DMTA and MT machines (for small cylinders) as well as the Instron (for the big cylinders) has been considered. The flow stress has be plotted as a function of strain rate at chosen values of the true compressive strain (at 5%, 20% and 30%) as presented in Annex D. By fitting a power law (1) through each data sat, the material parameters  $C_\sigma$  and  $N$  have been revealed as shown in Table 1.

Phase	Strain (%) for considered flow stress	$C_\sigma$ ( MPa s <sup>N</sup> )	$N$
Hardening	5	5.117	0.140
Saturation	20	8.681	0.209
Saturation	30	8.383	0.203

**Table 1:** Numerical values of the creep exponent  $N$  and the constant  $C_\sigma$  determined via power-law fitting of experimental data represented as log-log flow stress vs. strain rate (Annex D). These experiments were carried out with the Instron, DMTA and MT machines on compression specimens of two different nominal dimensions.

In the analysis process through which Table 1 was obtained it became apparent that a power law response is exhibited at room temperature, such that the flow stress  $\sigma$  scales with the strain rate  $\dot{\epsilon}$  according to the viscoplastic constitutive equation (1), since it provides a very good fit to the data. The average value obtained for the creep exponent  $N = 0.206$  at saturation is consistent with the deformation mechanism of power law creep. In the hardening phase the same process does not apply as  $N = 0.140$ .

### 4.3.2 Size effect observations

To observe the size effect, flow stress is plotted as a function of sample volume as presented in Fig. 9. For the purpose of this analysis, the total sample volume is assumed constant for each specimen undergoing deformation. The flow stress presents a higher scatter for the smaller specimens due to the small force magnitude associated with small strain and specimen dimensions. Nevertheless, it is evident that for all samples the average value of flow stress at 5% strain are approximately the same. This indicates there is no strengthening associated with a size effect. As in the uniaxial tension experiments (section 4.1), this phenomenon is justified by the absence of a strain gradient. Although not reproduced here, the same behavior was observed at various fixed strains and strain rates.

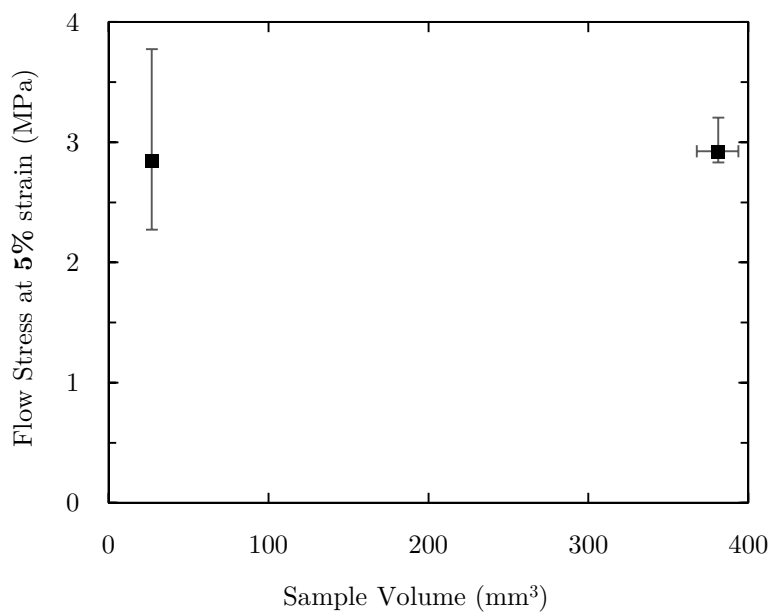


**Figure 9:** Stress flow at a fixed strain of 5% at a strain rate of 1E-02. The data is obtained by testing 20 cylinders of 2 sizes independently with the Instron, DMTA and MT machines. At a strain rate of 1E-02.

#### 4.4 Three-point bending

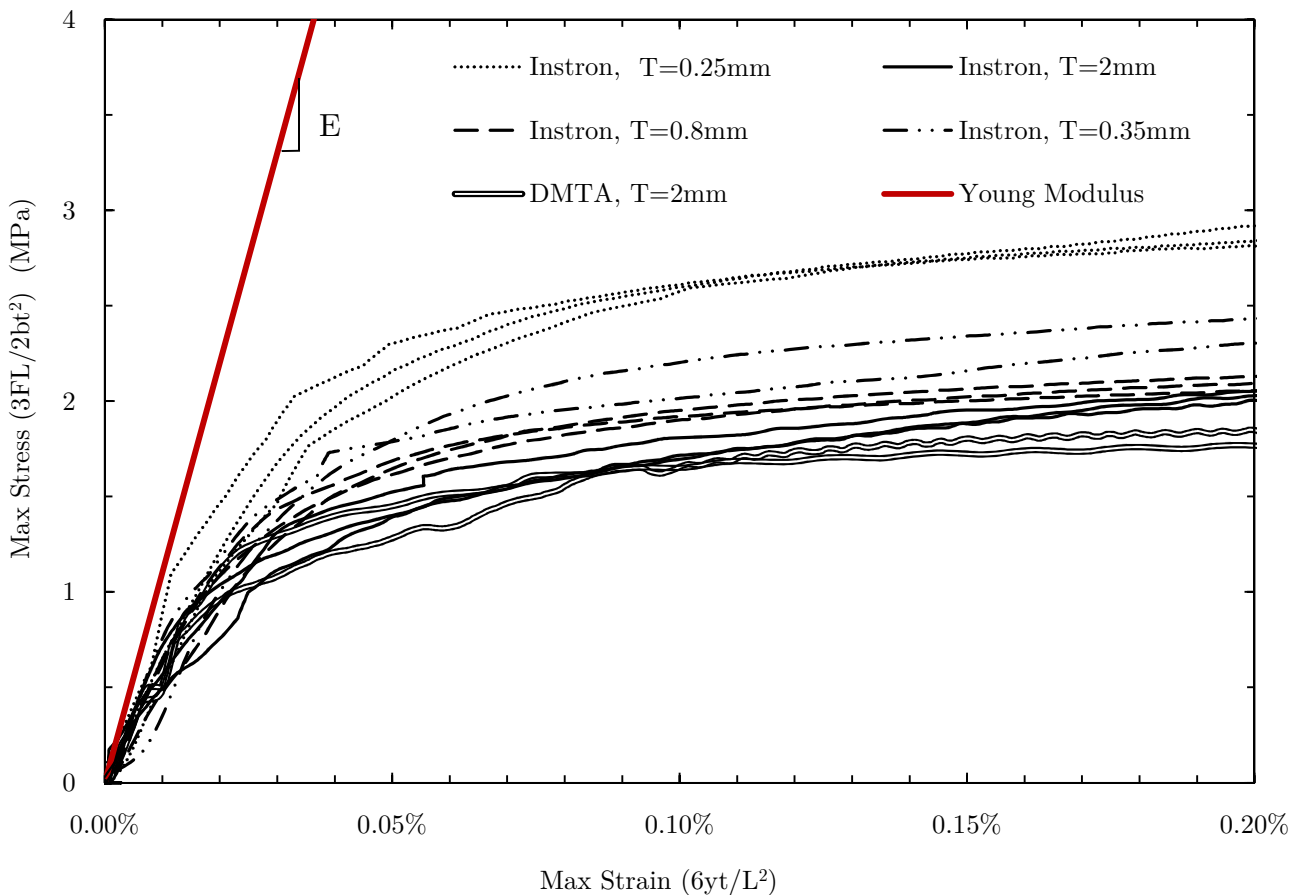


**Figure 10:** Results for all of the three-point bending tests showing the variation of maximum direct stress and strain (at the bottom of the beams). All specimens were tested at a nominal strain rate of  $1\text{E-}03$ .

The parameters of interest in these tests are the maximum stress and strain at the lower surface of the beam. Making the assumptions of the Euler-Bernoulli beam theory, these can be determined as  $\sigma_{max} = \frac{3PL}{2bt^2}$  and  $\varepsilon_{max} = 6 \frac{t}{L^2} \delta$ , where  $L = 20$  mm is the distance between outer supports,  $b$  and  $t$  are the width and thickness of each beam and  $\delta$  is the cross-head displacement. In order to eliminate the effect of strain rate variation between beams of different thicknesses, the cross head velocity has been adjusted for each test to ensure the same maximum strain rate at the mid-span lower surface of  $\dot{\varepsilon}_{max} = 10^{-3} \text{ s}^{-1}$ .

The true stress-strain curves shown in Fig. 10 clearly display a grouping associated with differential thicknesses, demonstrating the presence of a size effect. Several tests were also carried out with the DMTA using a fixture with the same dimensions to confirm the data. These showed the same results.

An attempt was made at determining the Young modulus from the linear-elastic portion of the curve, however the very small range of this region and precision limitations in manufacturing the beams meant the samples showed a ‘softening’ in the initial region as the test head made contact with the beam. Experimental data revealed  $E=7.71\pm 2.24$  GPa. This can be observed from Fig. 10 by comparing the experimental curves in the low strain region with the expected value of the slope  $E=12.74$  GPa.

To further evaluate this hypothesis, the model developed in section 3.2 has been compared with the experimental data and finite elements analysis simulation using the same power-law parameters determined previously ( $A=5.117$  and  $N=0.14$ ). Both the analytical model and the Abaqus simulation predicted an elevation of the flow stress which is at most 5% when comparing the maximum stress-strain curves of the thickest and thinnest beams (in the plastic regime). In contrast, the experimental data presented in Fig. 10 shows a much higher increase of more than 50% between the same curves. The model and simulation do not account for size effects, only strain rate effects. The fact that the curves corresponding beams of different thicknesses are close together and do not display the same grouping associated with differential strength with thickness eliminates the possibility that the behavior shown in Fig. 10 is a consequence of different strain rates and confirms that it is indeed due to a size effect.

Processing of the data carried out on indium samples of various different thicknesses, tested separately with the DMTA and Instron reveal a clear trend indicative of a size effect. This is presented in Fig. 11, where flow stress at fixed values of 0.1% strain and 0.2% strain are plotted with respect to specimen thickness and errors are quantified. The flow stress does not increase significantly from specimens of thickness 2 mm to those of thickness 0.8 mm.

However, when specimen thickness approaches the order of magnitude of the Indium length scale, there is a significant strength increase. Consequently, in contrast with tension (Fig. 5) and compression (Fig. 9), in microbending (Fig. 11), there are strain gradient plasticity effects determining a size effect. Furthermore, flow stress at 0.1% strain is consistently above that at 0.2% strain indicating the fact that the size effect is present at various levels of strain.

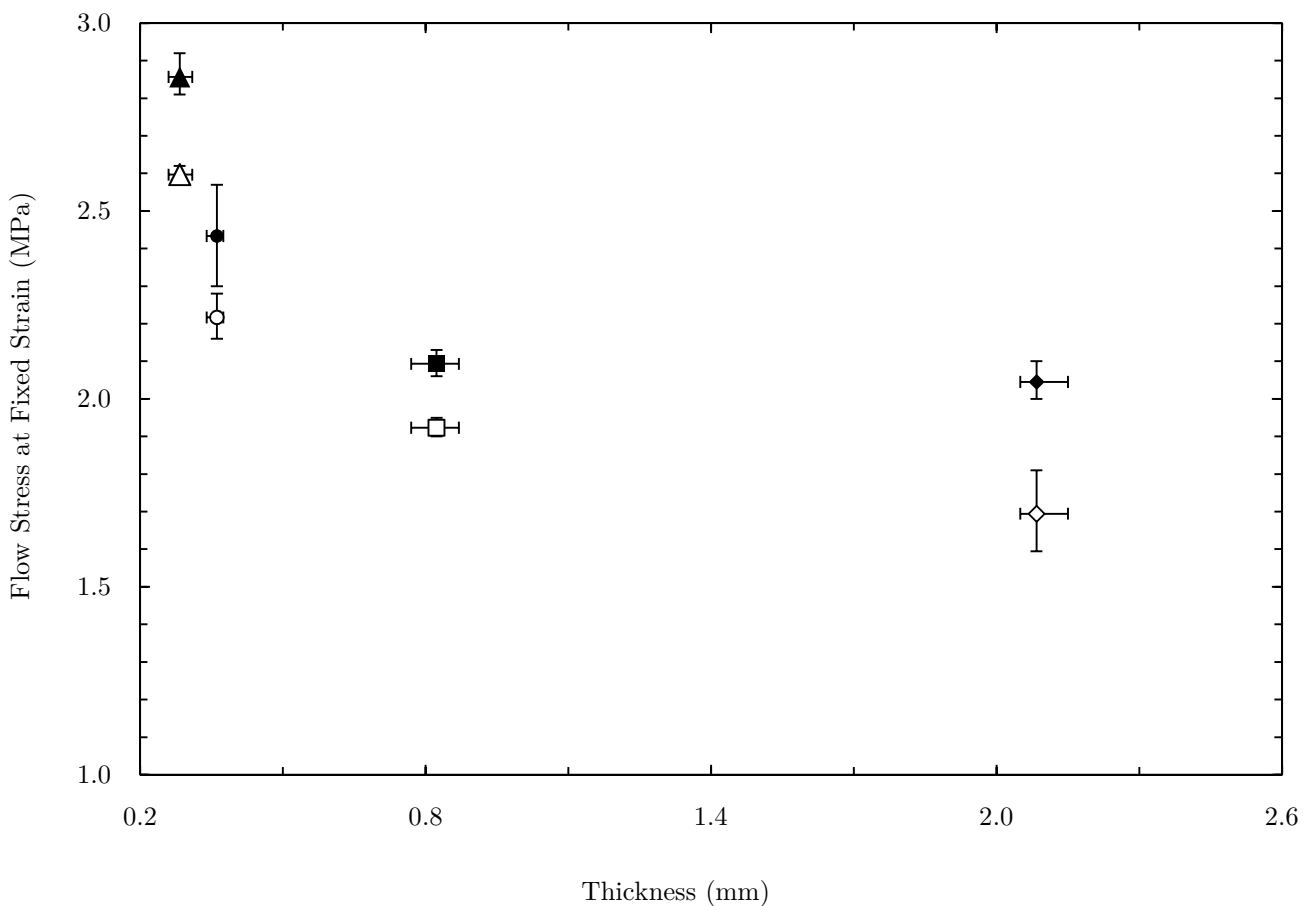


**Figure 11:** Flow stress at a fixed strain value of 0.1% (hallow) and 0.2% (filled) showing there is a size effect since thinner specimens present a higher flow stress at the same strain value. Experiments were carried out with the Instron and DMTA and results are consistent, their average is shown in the present figure.

#### 4.5 Vickers micro-hardness experiment

Measuring the diagonals ( $d$ ) of the indented shape through an optical microscope revealed the area of the indentation  $A_c = d^2/2$  and knowing the Vickers indenter geometry it was possible to determine the indentation depth as:

$$h = \frac{d\sqrt{2}}{4 \tan 68^\circ} \quad (19)$$

The hardness is defined as the hydrostatic pressure resisting indentation  $H = P_0/A_c$  where  $P_0$  is the force exerted in the indentation test and  $A_c$  is the area of contact between indenter and material, projected on the plane perpendicular to the applied load. Therefore:

$$h = \frac{1}{4 \tan^2 68^\circ} \frac{P_0}{h^2} \quad (20)$$

However, using just the diagonals means neglecting the phenomena where the indentation shape does not have sharp vertices and straight sides (e.g. sink-in, pile-up). By taking images of each indentation and finding the number of pixels within the area it was possible to improve accuracy. Finally, the potential error induced by calculating the area  $A_c$  from the values of the diagonals has been quantified and found to be within the error bounds of the experiments. The average error in the area is of the order of  $\pm 10794.5 \mu\text{m}^2$  (6.7%) leading to an error in estimating the depth of approximately  $\pm 1.8 \mu\text{m}$  (3.4%) and for hardness  $\pm 0.7 \text{ MPa}$  (6.8%).

Results for hardness versus indent depth  $h$  are plotted in Fig. 12; each datapoint represents the average of five tests. In each of these experiments  $t_1$  was held fixed at 10 s, while the maximum load  $P_0$  was between 0.245 N and 10 N. It is assumed that no pile-up occurs, such that the indentation depth  $h$  is related to the footprint diagonal  $d$  by the geometrical relation  $h = d/6.74$ . Since hardness is observed to increase with diminishing indent depth (below 90  $\mu\text{m}$ ), a size effect is present. This can be interpreted in terms of strain-gradient plasticity theory: the smaller the indent, the larger the strain gradient and thereby the higher the hardness.

It is difficult to interpret the indentation results at room temperature, since indium has a high strain rate sensitivity (as shown in section 4.3.2) and the imposed strain rate beneath the indenter increases with diminishing indenter size (at a fixed indentation velocity). Consequently, additional analysis is needed in order to determine whether a true size effect exists or whether the increased hardness with diminishing depth is simply a consequence of strain rate sensitivity. This can be achieved through a comparison with the analytical model in section 3.1.

In generating the analytical model presented in Fig. 12, the values previously established (section 4.3.1) for  $C_\sigma$  and  $N$  in the saturation phase were used. Indium can be assumed perfectly plastic since  $\nu = 0.4498$  [20, p. 1201], thus  $C_H = 3$ . The load history is presented in Fig. 1 giving  $t_0 = 2$  s and  $t_1 = 7$  s. Finally the model (8) was fitted to the data for high indentation depths ( $>80$   $\mu\text{m}$ ) to obtain the remaining material constant  $C_\varepsilon = 0.84$ .

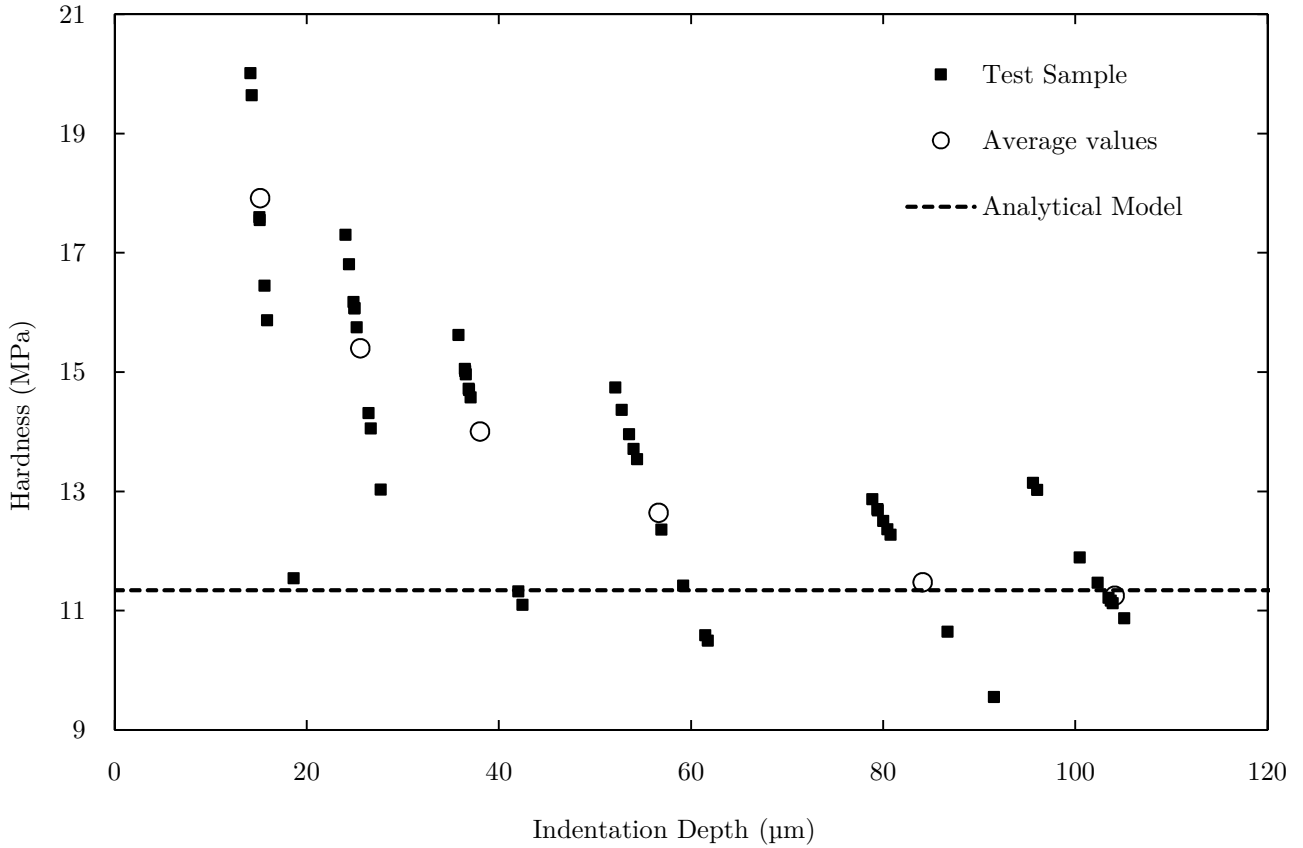


**Figure 12:** Indentation depth versus hardness for Vickers indentation of Indium at room temperature. Points line-up along lines of constant load for: 10, 24, 50 100, 200, 300, 500, 1000 grams of force.

The model predicts that the hardness versus time response is independent of load level, whereas the data reveals a pronounced size effect as the measured hardness increases by approximately 50% when  $P_0$  is decreased from 1.96 N to 0.245 N. Observing Fig. 12, the indent depth reduces from  $\sim 70$   $\mu\text{m}$  to  $\sim 30$   $\mu\text{m}$  with this reduction in load. The predicted response, absent any size effect, lies somewhat below the measured responses. This difference increases for larger indentation depths, which can be reconciled by the presence of strain-gradient strengthening.

#### 4.6 Constant load indentation (creep) experiment

Fig. 14 presents the indentation depth variation with time, for four values of  $P_0$ . As expected from a creeping material, depth  $h$  increases with time for all values of the applied load, while the rate  $\dot{h}$  decreases with increasing time. After an initial transient phase, the rate  $\dot{h}$  attains an approximately constant value; this steady-state rate increases with the load  $P_0$ .

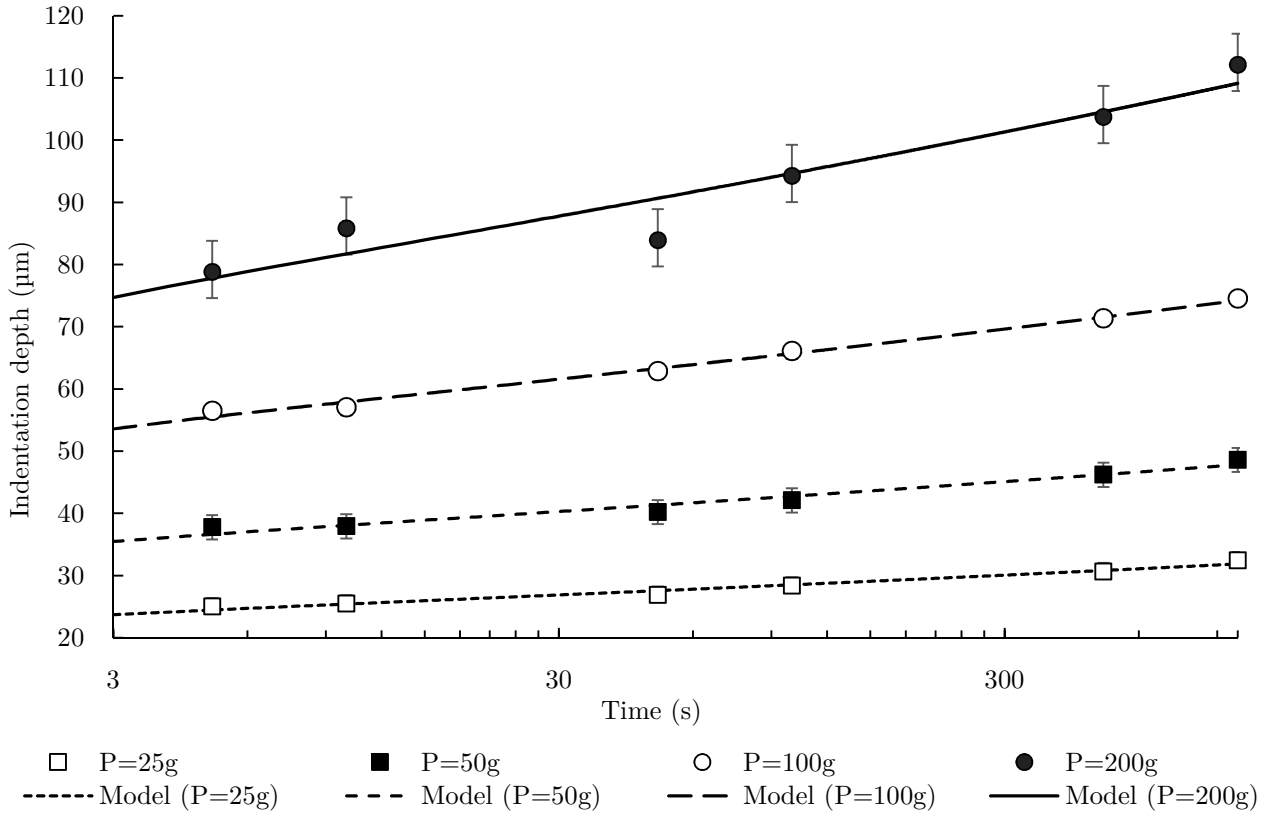


**Figure 13:** Indentation depth versus time history for Vickers indentation of Indium at room temperature, for four values of the applied load. The model (6) has been fitted to each loading case. Data is averaged between three experiments and errors are quantified.

By fitting the model developed in section 3.1 to the data presented in Fig. 13, the numerical values of the creep exponent of Indium ( $N$ ) and of the constant product  $C_H C_\sigma$  have been obtained for each value of the maximum applied load  $P_0$ . These have assembled in Table 2.

$P_0$ (mN)	$N$	$C_H C_\sigma$ (MPa s <sup>N</sup> )
245.3	0.096	25.53
490.5	0.097	22.90
981	0.106	20.56
1962	0.123	22.19

**Table 2:** Numerical values of the creep exponent  $N$  and the constant  $C_H C_\sigma$  determined via least-square fitting of (6) to the experimentally determined indentation depth vs. time histories in Fig. 13, for  $t_0 = 2s$  and  $C_A = 24.5$ .

An additional point in support of this interpretation of the experimental data can be made by comparing the indentation depth versus time histories presented in Fig. 13 to the predictions of the analytical model developed in section 3.1. This anticipates that the time variation of  $h$  should follow equation (6). Least-squares fits of this equation to the data presented in Fig. 13 were produced and experiments and predictions revealed a close match. For the higher load used the match is not as good due to the higher scatter in experimental data, caused by pile-up and sink-in phenomena associated with the indentation procedure.

Furthermore, it is possible to observe that the extracted values of the creep exponent  $N$  in Table 2 are substantially smaller than the value  $N = 0.206$  determined via uniaxial compression experiments on large samples [17] shown in Table 1 (section 4.3.1). The creep exponent determined from the least-squares fits approaches 0.2 for increasing applied maximum loads. A comparison of the data in Fig. 12 to the predictions of (8) reveals:

- For a given applied maximum load  $P_0$ , the accuracy of (6) is worse at low indentation depths than at high  $h$ ; in particular, at small  $h$  the predicted material response is softer than the observed response.
- The accuracy of (8) increases for higher applied loads (and therefore for larger  $h$  values), as quantified by measuring the fit-to-data error as a function of time at each applied  $P_0$ .

The discussion above suggests that the analytical model developed in section 3.1, which does not account for size effects in the material response, is adequate to predict the indentation depth versus time histories for a power-law creeping material at high loads (and indentation depths); in contrast the model is not accurate, and predicts a softer material response, at small loads (and indentation depths). This supports the notion of a stronger observed material response at low indentation depths.

The measured indentation depth versus time histories reported in Fig. 13 can alternatively be presented in terms of  $H$  versus time, for each choice of  $P_0$ , as plotted in Fig. 14. It is found that the hardness increases with diminishing load  $P_0$ , at any given time. The analytical model in section 3.1 reveals that this increased hardness is associated with a strain gradient effect. Thereby an intrinsic size effect is present in the creep regime.

The simple model developed in section 3.1 does not account for material length-scale and size effects in predicting the Indium response to plastic deformation. Equation (7) considers hardness  $H$  is independent of the maximum applied load and only depends on time.

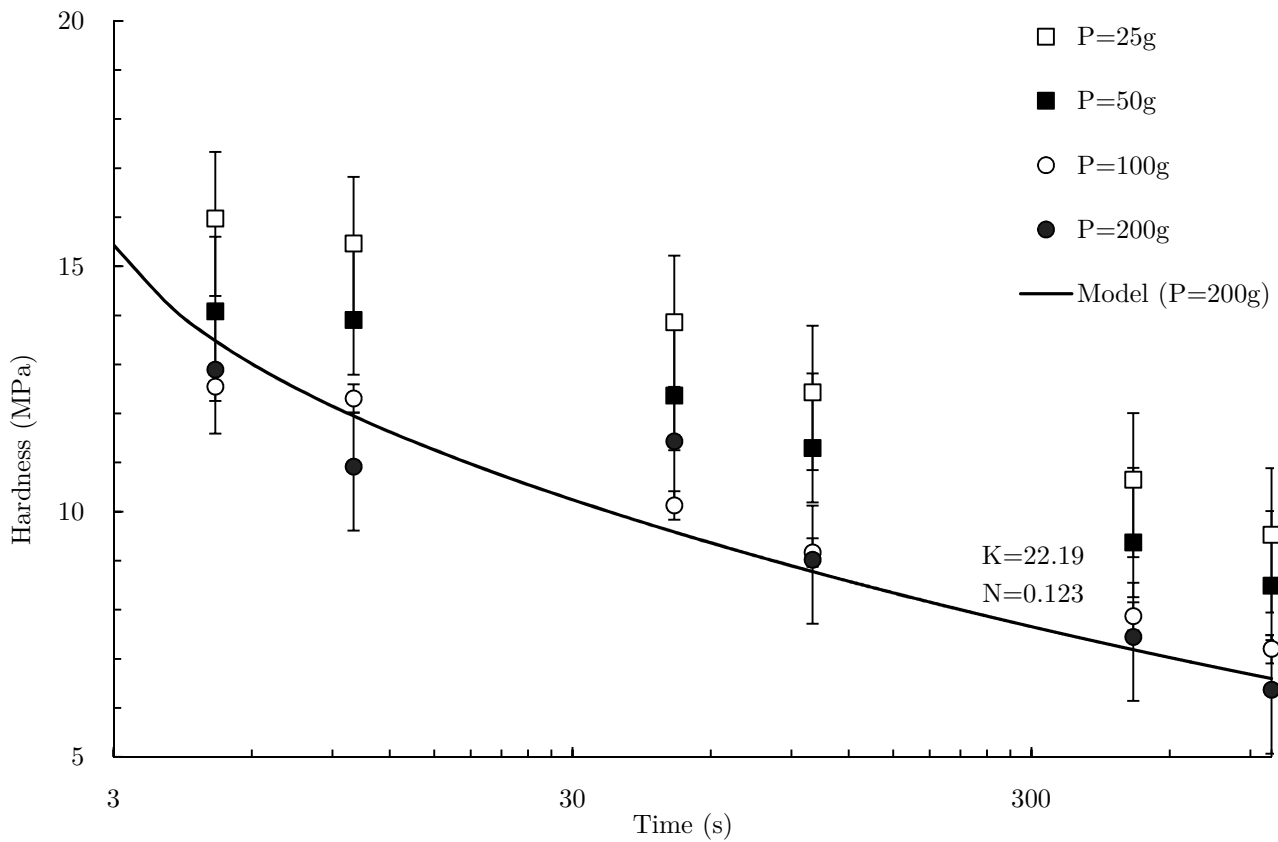


**Figure 14:** Hardness versus time history for Vickers indentation of Indium at room temperature, for four values of the applied load. Data is averaged between three experiments (at each load and  $t_1$  value). The model (7) has been fitted to the most applicable loading case (i.e. the highest load).

Fitting the model to the case where it is most applicable, at high indentation depth, reveals a relatively good match to experimental data, as presented in Fig. 14. This is because it accounts for the creep phenomena and at large depths size effects are relatively small. However, when comparing it with the values obtained at smaller loads, where the indentation depth approaches the indium length scale, the model does not work well anymore.

#### 4.7 Instrumented indentation experiment

Experimental results from the depth-sensing test carried out with the Instron and DMTA machines were processed together to reveal they are in accordance. In total there 14 experiments were carried out on both the thick and thin depth sensing specimens. Fig. 15 presents the variation of the measured load with the penetration depth of the Vickers indenter.

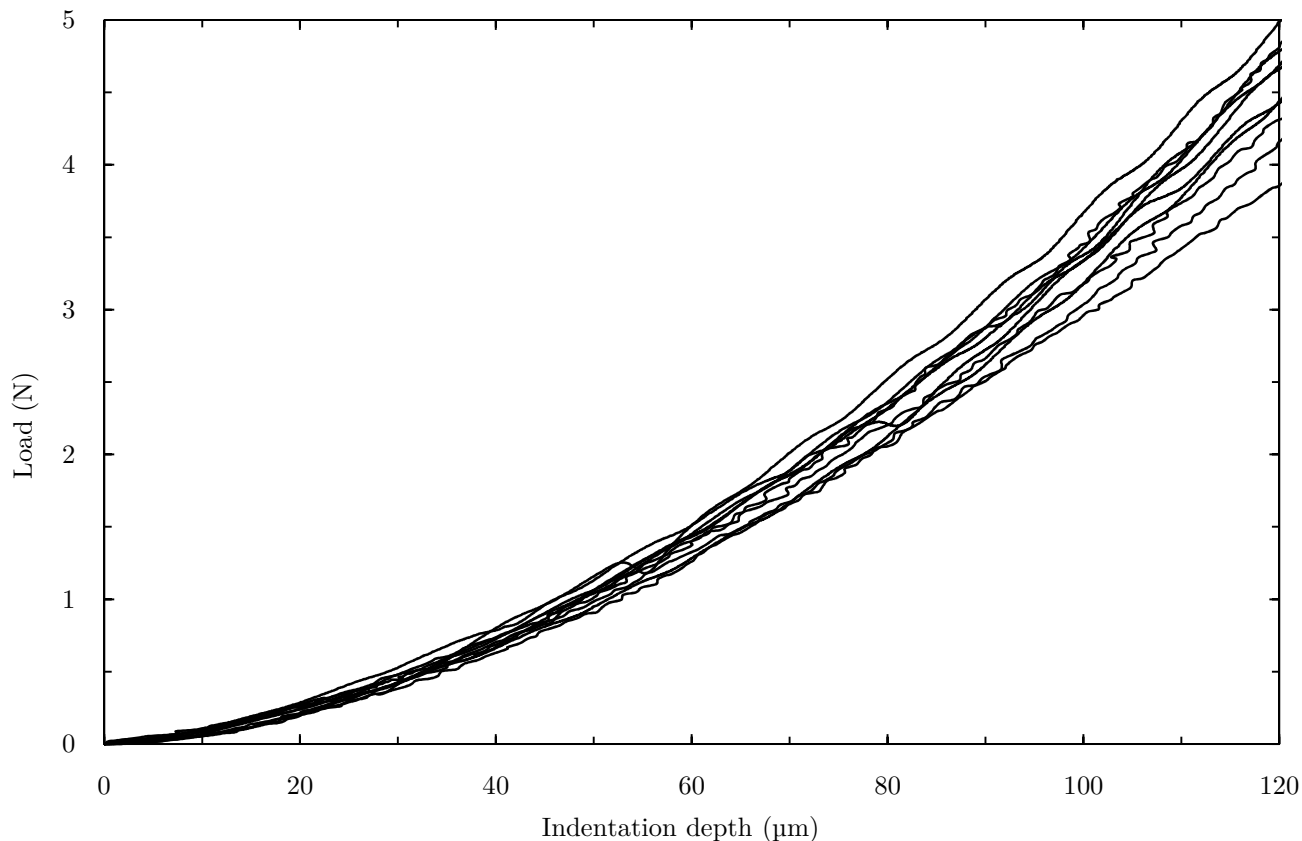


**Figure 15:** Load versus indentation depth for Vickers depth sensing indentation tests carried out with the Instron and DMTA machines.

The load resolution obtained with the DMTA (0.1 mN) was comparable with that of the Instron (10 mN). To obtain displacement data in the Instron test, an Imetrum non-contacting video extensometer was used. This gave a noise level of 300 nm. The DMTA displacement resolution was far superior at just 1 nm. Yet this did not affect the data obtained in a significant way hence both curves showed the same behavior and thus were plotted together in Fig. 15.

After determining the hardness variation with indentation depth, a moving average of all 14 experiments was computed and plotted in Fig. 16. Using this curve it was possible to fit the analytical model developed in section 3.1 for depths higher than 100 μm, considering a value for the stress exponent of  $N = 0.206$ . This value is appropriate for the saturation phase of the indentation creep, as demonstrated in section 4.3.1. It was thus possible to obtain the material constant  $K_d = 78.76$ .

Analysing Fig. 16 it is possible to observe that the hardness reaches a ‘steady-state’ value of 11 MPa at a depth of over  $\sim 100 \mu\text{m}$ . This is consistent with the hardness obtained in the microhardness experiment (Fig. 12, section 4.5) for the same depth, associated with the saturation phase. For depths lower than  $\sim 100 \mu\text{m}$ , the hardness  $H$  is a function of the maximum penetration depth  $h$  and  $H$  increases with decreasing  $h$ .

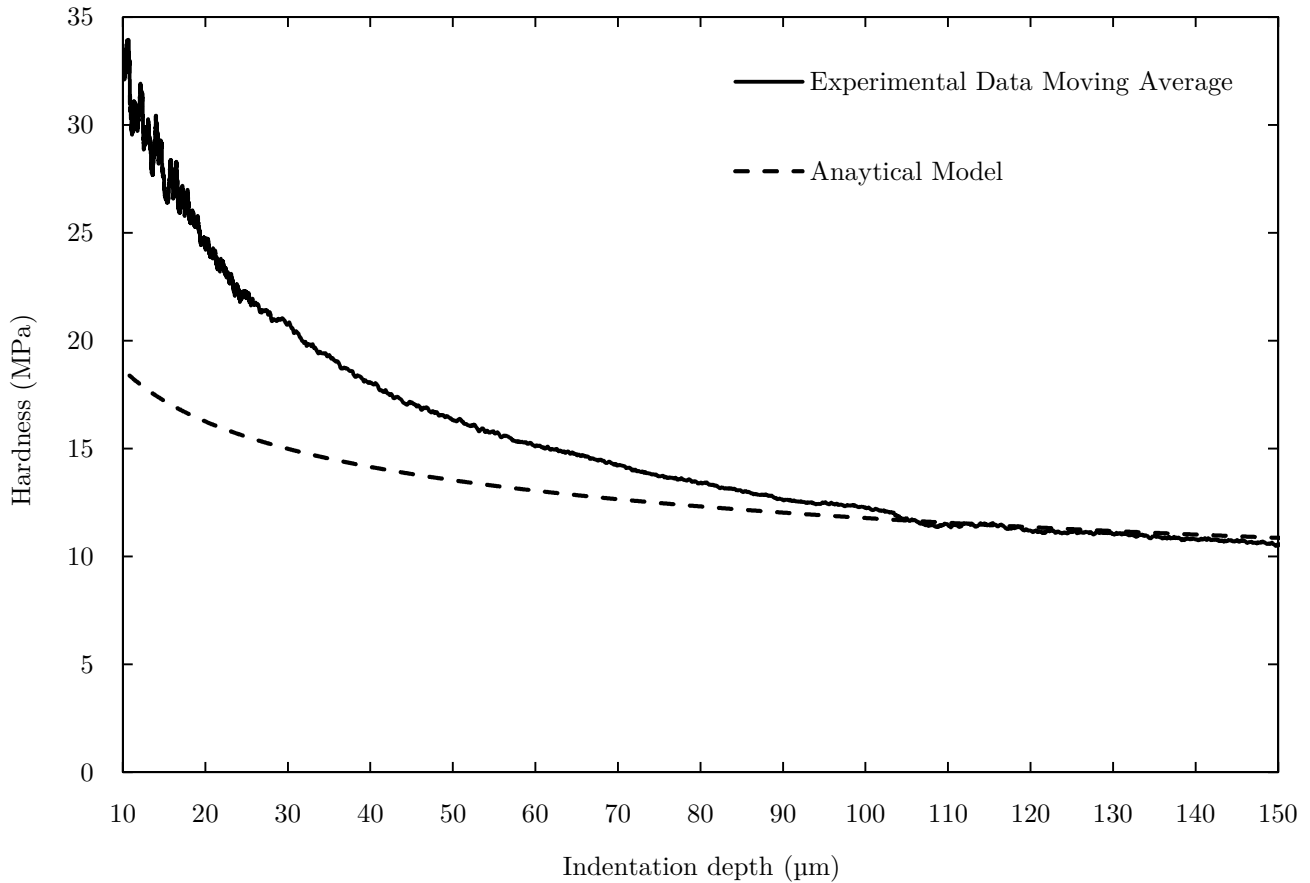


**Figure 16:** Hardness variation with indentation depth for Vickers depth sensing indentation tests carried out with the Instron and DMTA. The model (8) has been fitted to the moving average of the experimental data.

The analytical model (8) developed in section 3.1 has been plotted in Fig. 16 using the material constants found in the previous sections. It shows a good fit, within 4.5% of the experimental, for  $h > 90 \mu\text{m}$ . The model no longer matches the data for lower values of  $h$ . This is explained by the fact that the model accounts just for creep and not size effects. It is evident that for  $h < 90 \mu\text{m}$  the divergence of the two curves indicates the presence of a size effect.

A number of other factors might lead to this phenomenon, each associated with a length-scale in the indentation problem. A roughness comparable to the indentation depth, the presence of inclusions, a fine-grained material, the existence of a hard boundary layer, would introduce a length-scale in the problem and might be responsible for the indentation size effect.



Since the fit for the lower strain data is better (lower scatter), this dataset was used to identify the length scale as  $l_{FH} = 93.34 \mu\text{m}$  and the yield stress as  $\sigma_{y,FH} = 1.55 \text{ MPa}$ . Finally the yield strain is found from (25) as  $\varepsilon_{y,FH} = 1.4\text{E-}04$ .

Subsequently, through fitting the model developed in Annex C2 to the depth sensing indentation data presented in Fig. 16, considering data for depths higher than  $5 \mu\text{m}$  in order to avoid the large scatter found at very small depths, it is possible to obtain the curve presented in Fig. 18. Therefore, the length scale can be calculated as:  $l_{NG} = 85.21 \mu\text{m}$ .

To find the yield strain of the material it is possible to use the macroscopic hardness parameter determined as  $H_0 = 5.1256 \text{ MPa}$  from (29), the empirically determined relationship between hardness and yield stress from Tabor [19] as well as the Young Modulus definition:

$$\varepsilon_{y,NG} = \frac{\sigma_{y,NG}}{E} = \frac{cH_0}{E} \quad (22)$$

where  $c$  was determined by Tabor as 0.34 for metals and  $E$  for Indium is 11 GPa [21], thus  $\varepsilon_{y,NG} = 1.5\text{E-}04$ . Alternatively, one could assume the yield strain determined from microbending is more applicable than that referring to metals in general and determine the Tabor factor for indium as 0.3 [19]. However for the purpose of developing Fig. 19,  $c$  is kept as 0.34.

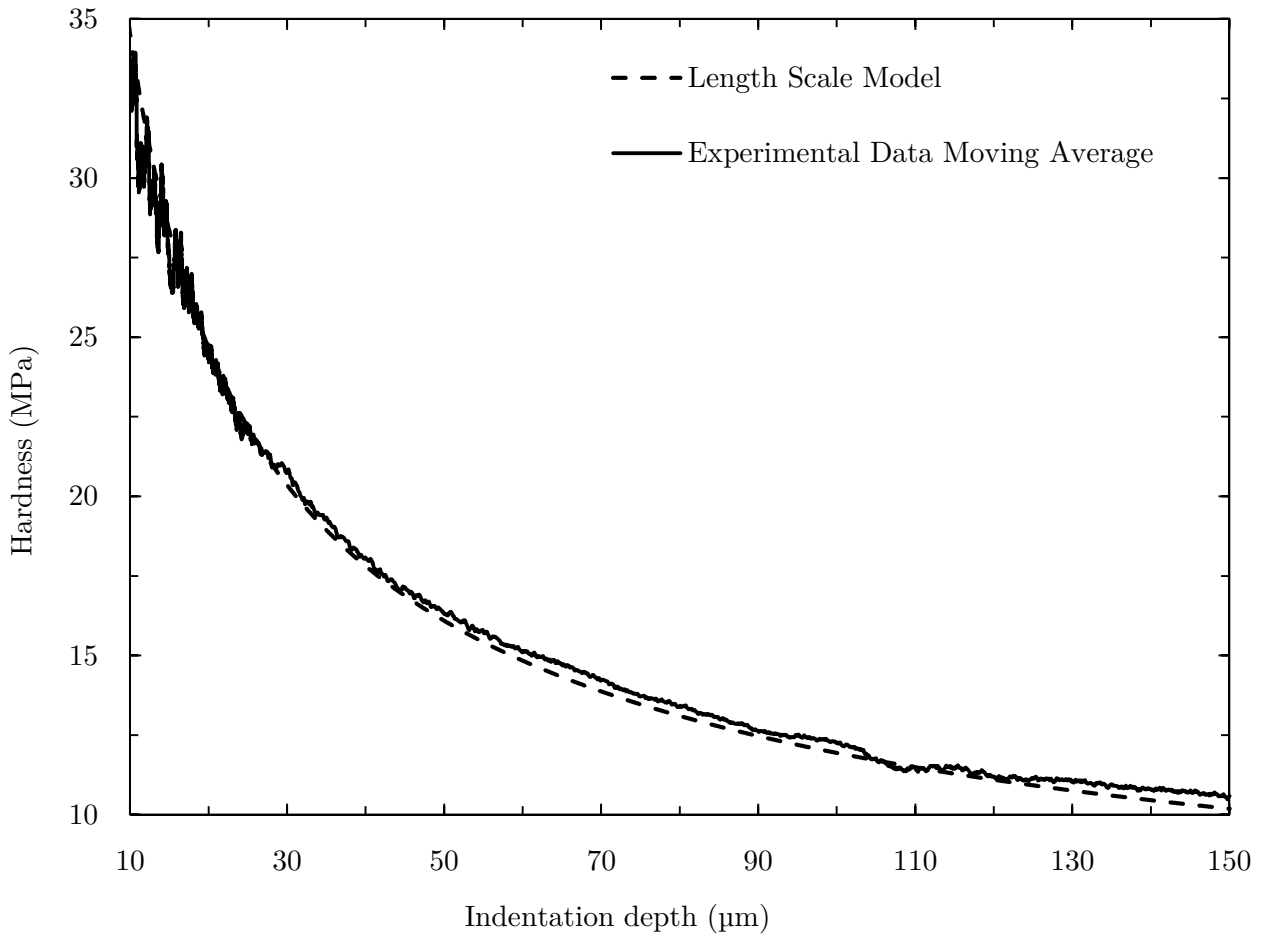


**Figure 18:** Fitting of the model developed in Annex C2 to the experimental depth sensing data.

These results are also consistent with the observations made in the Vickers microhardness and depth sensing experiments (section 4.5, Fig. 12 and section 4.7, Fig. 16) where the hardness increases when compared to the ‘indentation of a power-law creeping metal absent any size effects’ model for depth values below 90  $\mu\text{m}$ . Therefore it is possible state with a high level of certainty that the length scale of indium is  $89.27 \pm 4.07 \mu\text{m}$  and its yield strain is  $1.5\text{E-}04$ . The result is plotted in Fig. 19 along with the length scales obtained for various metals by other authors. Fitting all data points reveals indium has a significantly larger length scale than other metals previously studied.

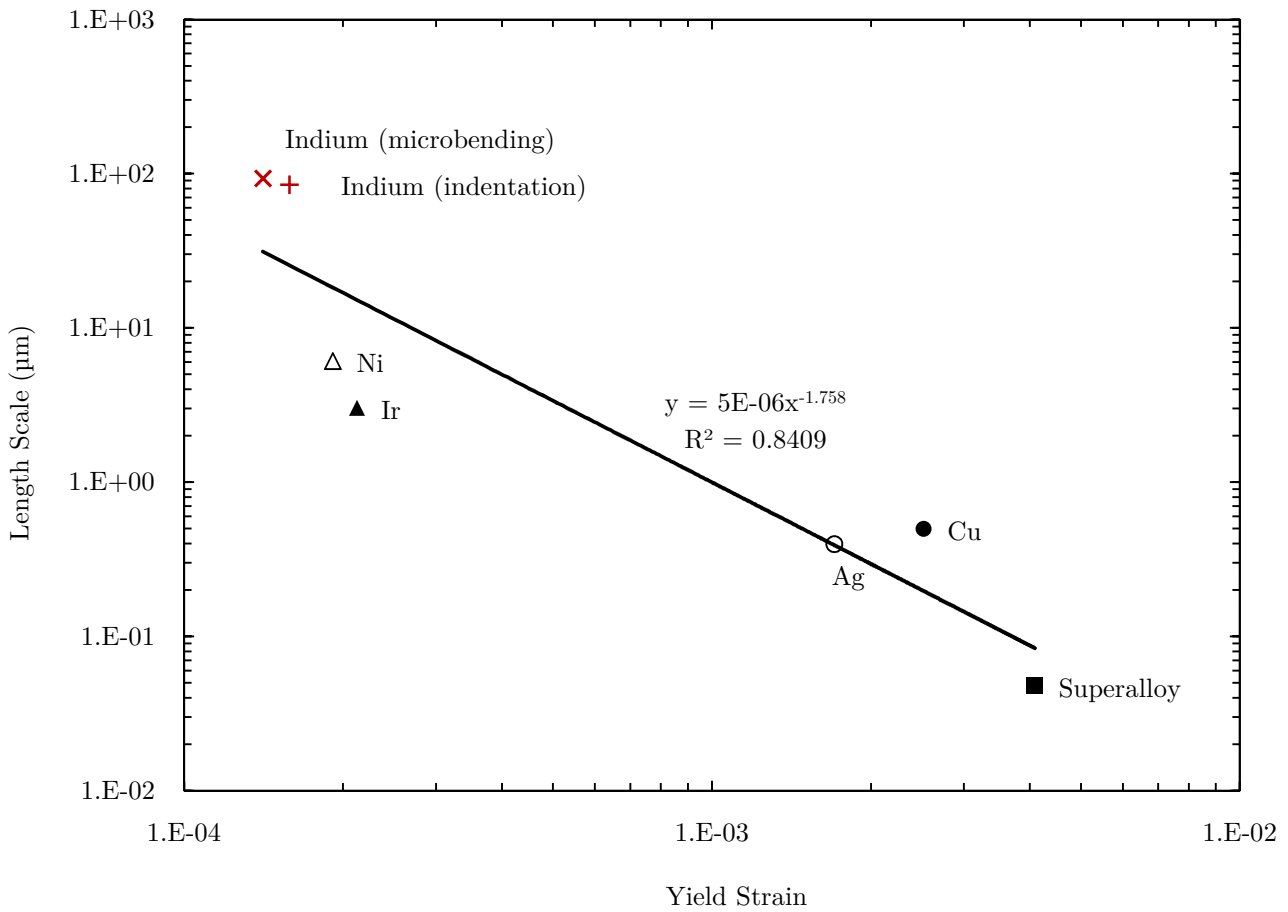


**Figure 19:** Extrapolation of the Indium length scale results obtained in this study and the data compiled by Evans and Hutchinson [4] based on the results achieved for Ni [4], Ir [8], Ag [21], Cu [22], and a Superalloy [20].

## 5. Conclusion

The primary objective of the paper, the analysis of mechanical properties and specimen size effects of high purity Indium at room temperature (in the creep regime), has been achieved through uniaxial tension, uniaxial compression, micro-indentation and three-point bending tests.

Vickers indentation experiments revealed that the hardness increased with decreasing indentation depths at room temperature (22°C). In order to help interpret this observation in the creep regime, an analytical indentation model has been developed in section 3.1, absent any strain-gradient strengthening. Having determined the mechanical response of Indium at room temperature, through a suite of tests, it was possible to conclude with the analysis of the graphs and draw a comparison with the analytical model. This revealed the presence of a size effect in indentation and bending, consistent with previous studies [2-9]. In fact, the hardness doubled as the indentation depth decreased from 60  $\mu\text{m}$  to 10  $\mu\text{m}$ . The model predicts an indentation response independent of applied load, whereas the data reveals an increasing hardness with diminishing load. It is conjectured that the source of the size effect is the presence of additional geometrically necessary dislocations with increasing strain gradient as postulated by Ashby [2]. These additional dislocations act as barriers to dislocation creep, and climb is required in order to overcome them. A stress exponent of  $N = 0.206$  was determined, in line with the values found by other authors employing different experimental methods [14], [15], [16].

The uniaxial compression experiments revealed a strain rate sensitivity. In order to aid interpretation of the creep and depth-sensing data and to establish the existence of a size effect, an analytical model is developed for the indentation response of a power-law creeping solid absent a size effect. Upon comparing the models with the experimental data a size effect was observed for indentations depths below 90  $\mu\text{m}$ .

No evidence of a size effect was detected in both uniaxial tension and compression, which is to be expected due to the lack of a hardening associated with plastic strain gradients.

In the uniaxial tension experiment, from the linear portion of stress-strain curves, the Young modulus at room temperature was found to be 12.03 GPa which is consistent within 5.6% of established results [20]. Due to instrument and manufacturing precision limitations, the modulus could not be determined from the linear-elastic portion of the compression and microbending tests as well as from the unloading portion of the depth-sensing experiment.

Finally, the length scale and yield strain of Indium were found to be  $\sim 90$   $\mu\text{m}$  and  $\sim 1.5\text{E-}04$  respectively. To achieve this, plasticity theories (Fleck-Hutchinson and Nix-Gao) were applied to the microbending and indentation data respectively. The values obtained are consistent with the microbending and microhardness experimental results. Finally, the length scale was found to be significantly higher than that reported for other metals.

## 6. Future improvements: cryogenic temperature experiments

Although beyond the scope of the academic paper, an attempt was made at replicating the depth sensing and compression experiments at cryogenic temperatures. This would bring indium out of the creep regime and act as a second tool in analyzing the size effect, in addition to the analytical models developed. To achieve this a custom fixture was designed and printed in ABS to hold a Pyrex glass container and fit it to the 100 N load cell of the Instron (technical drawings are included in Annex B6 & B7). The laser extensometer was used to track displacement. The specimens used were a selection of pristine samples from the same batch manufactured for the room temperature experiments. Liquid nitrogen ( $\text{LN}_2$ ) was chosen as a coolant since it is commonly available and can bring Indium near its boiling temperature ( $-196^\circ\text{C}$ ) upon submersion. A debit control device was built to maintain a constant level of  $\text{LN}_2$  within the test compartment (Annex B8).

### Uniaxial Compression $\text{LN}_2$ Experiments

Six tests were completed at a strain rate of  $10^{-2} \text{ s}^{-1}$  out of which 3 were successful. This is due to the challenges associated with this experimental setup, the laser extensometer frequently lost tracking because of icing and  $\text{LN}_2$  vapours. The average curves of both room temperature and successful  $\text{LN}_2$  experiments are presented in Fig. 20. Because data has been obtained for just one strain rate it is of limited use. However it does reveal a significant increase in the strength of the material with trues stress achieving values twice as large at  $\text{LN}_2$  temperatures at the same strain level.

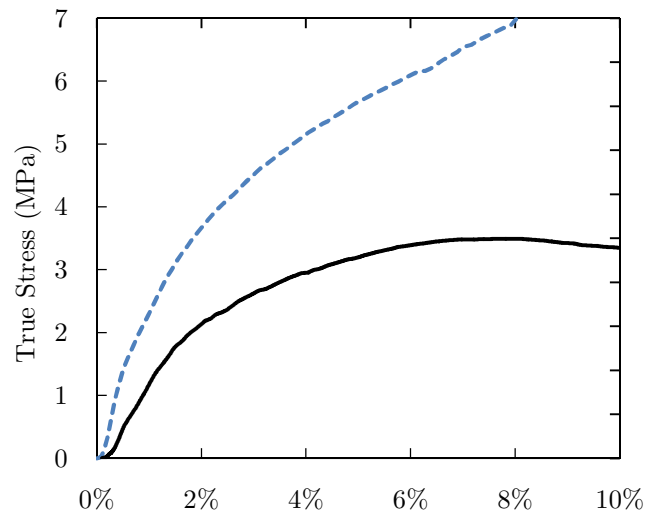


**Figure 20:** Comparison of the uniaxial compression response of indium in the non-creep regime ( $\text{LN}_2$  temperature, dotted line) and in the creep regime (room temperature, continuous line).

### Depth-Sensing $\text{LN}_2$ Experiments

Replacing the upper compression fitting with a Vickers indenter and making use of the same experimental setup as for the cryogenic compression tests, depth sensing experiments were carried at cryogenic temperatures on the same flat samples, 5 mm in thickness.

Due to the challenges associated with this experiment, out of 20 tests carried out, 5 were successful. As can be seen in Fig. 21, there was a large scattered in the data obtained at low indentation depths when compared to the room temperature results. This was because the moment when the indenter contacts the sample was hard to determine accurately.

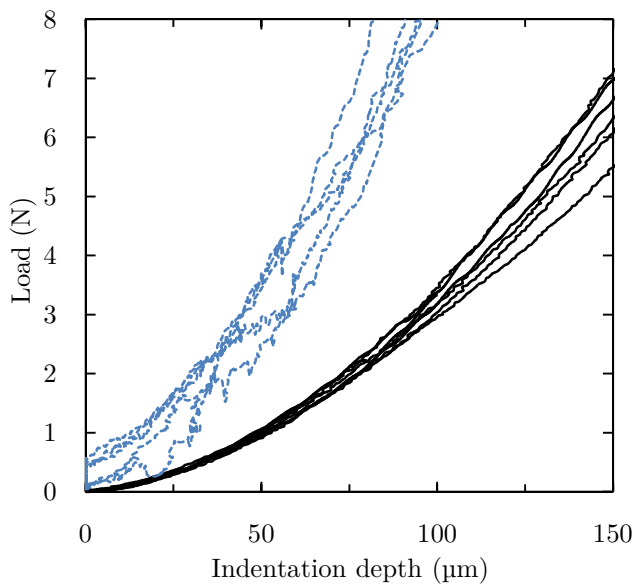


**Figure 211:** Comparison between the depth sensing response of indium in the non-creep regime (LN<sub>2</sub> temperature, blue dotted line) and in the creep regime (room temperature, black continuous line).

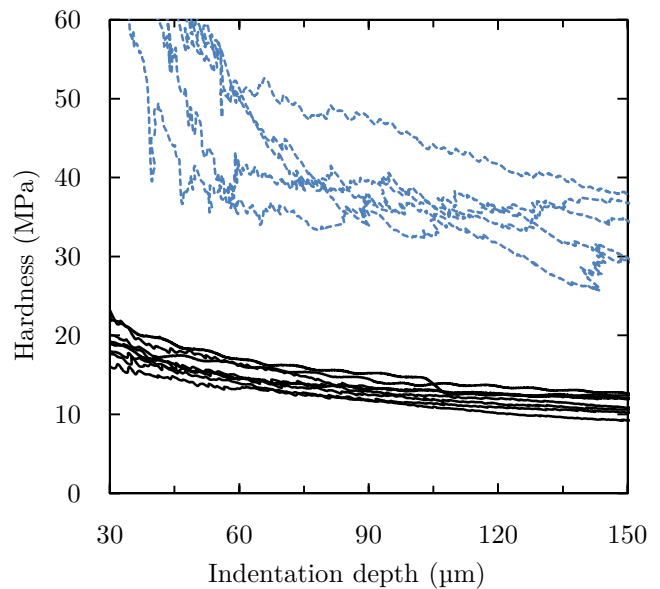


**Figure 232:** Hardness variation with depth for the non-creep regime (LN<sub>2</sub> temperature, blue dotted line) compared to that in the creep regime (room temperature, black continuous line).

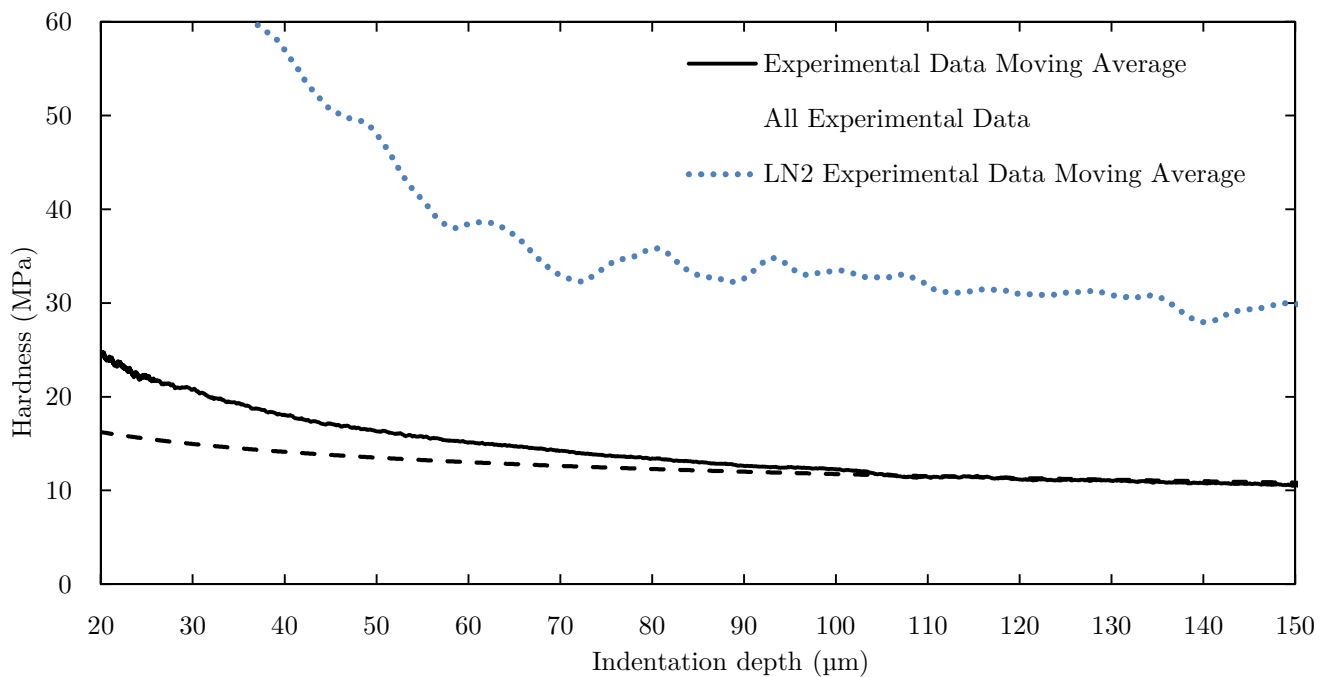


**Figure 223:** Comparison of the average experimental data in the creep and non-creep regimes. The analytical model has been fitted to the room temperature data.

Through averaging the experimental data displayed in Fig. 22 it is possible to observe a general trend in the hardness variation with depth (Fig. 23). The hardness presents little variation for  $h > 100 \mu\text{m}$ . When approaching the length scale of indium and for values below  $90 \mu\text{m}$  hardening is observed in the non-creep regime as well, yet it appears to start at lower depths than in the creep regime. Although promising, these experiments should be performed again with the DMTA Analyser to obtain more accurate results, all other experiments in this study can also be carried out at cryogenic temperatures to characterise indium in the non-creep regime.

## References

- [1] C. Scharlemann, A. Genovese, N. Buldrini, R. Schnitzer, M. Tajmar, "Status of the Indium FEEP Micropropulsion Subsystem Development for LISA Pathfinder," in *International Electric Propulsion Conference*, Florence, Italy, 2007 .
- [2] M. F. Ashby, "The deformation of plastically non-homogenous materials," *Philosophical Magazine*, no. 21, p. 399–424, 1970.
- [3] N. A. Fleck, G. M. Muller, M. F. Ashby and J. W. Hutchinson, "Strain gradient plasticity: theory and experiment," *Acta Metallurgica et Materialia*, no. 42, p. 475–487, 1994.
- [4] J. S. Stolken and A. G. Evans, "A microbend test method for measuring the plasticity length scale," *Acta Materialia*, no. 46, p. 5109–5115, 1998.
- [5] A. G. Evans and J. W. Hutchinson, "A critical assessment of theories of strain gradient plasticity," *Acta Materialia*, vol. 5, no. 57, pp. 1675-1688, 2009.
- [6] N. A. Stelmashenko, M. G. Walls, L. M. Brown and Y. V. Milman, "Microindentation on W and Mo oriented single crystals: an STM study," *Acta Metallurgica et Materialia*, no. 41, p. 2855–2865, 1993.
- [7] K. W. McElhaney, J. J. Vlassak and W. D. Nix, "Determination of indenter tip geometry and indentation contact area for depth-sensing indentation experiments," *Journal of Materials Research*, no. 13, p. 1300–1306, 1998.
- [8] A. M. a. F. N. Poole W.J., "Hardness tests on annealed and work-hardened copper polycrystals," *Scripta Materialia*, no. 34, p. 559–564, 1996.
- [9] J. G. Swadener, E. P. George and G. M. Pharr, "The correlation of the indentation size effect measured with indenters of various shapes," *Journal of the Mechanics and Physics of Solids*, no. 50, pp. 681-694, 2002.
- [10] N. A. Fleck and J. W. Hutchinson, "A phenomenological theory for strain gradient effects in plasticity," *Journal of the Mechanics and Physics of Solids*, no. 41, p. 1825–1857, 1993.
- [11] N. A. Fleck and J. W. Hutchinson, "Strain gradient plasticity," *Advances in Applied Mechanics*, vol. 33, p. 295–361, 1997.
- [12] N. A. Fleck and J. R. Willis, "A mathematical basis for strain-gradient plasticity theory – Part I: Scalar plastic multiplier.," *Journal of the Mechanics and Physics of Solids*, no. 57, pp. 161-177, 2009.

- [13] N. A. Fleck and J. R. Willis, "A mathematical basis for strain-gradient plasticity theory – Part II: Tensorial plastic multiplier.," *Journal of the Mechanics and Physics of Solids*, no. 57, pp. 1045-1057, 2009.
- [14] J. Weertman, "Creep of Indium, Lead, and some of their alloys with various metals," *Transactions of the Metallurgical Society of AIME*, no. 218, pp. 57: 1045-1057, April 1960.
- [15] B. N. Lucas and W. C. Oliver, "Indentation power-law creep of high-purity Indium," *Metallurgical and Materials Transactions*, no. 30A, pp. 601-610, 1998.
- [16] M. Galli and M. L. Oyen, "Creep properties from indentation tests by analytical and numerical techniques," *International Journal of Materials Research*, no. 100, pp. 954-959, 2009.
- [17] A. F. Bower, N. A. Fleck, A. Needleman and N. Ogbonna, "Indentation of a power law creeping solid," *Proceedings of the Royal Society A*, no. 441, pp. 97-124, 1993.
- [18] M. J. Mayo and W. D. Nix, "A micro-indentation study of superplasticity in Pb, Sn, and Sn 38% wtPb," *Acta Metallurgica*, no. 36, p. 2183, 1988.
- [19] D. Tabor, *The Hardness of Metals*, Oxford: Clarendon Press, 1951.
- [20] ASM International, "Properties and Selection: Nonferrous Alloys and Special-Purpose Materials," in *ASM Handbook Volume 2*, ASM International, 1990, pp. 1099-1201.
- [21] I. M. Hutchings, "The contributions of David Tabor to the science of indentation hardness," *Journal of Materials Research*, vol. 24, no. 3, p. 583, 2009.
- [22] G. Taylor, "Plastic strain in metals," *Institute of Metals*, vol. LXII, pp. 307-324, 1938.
- [23] K. Hemker, B. Mendis and C. Eberl, "Characterizing the microstructure and mechanical behavior of a two-phase NiCoCrAlY bond coat for thermal barrier systems," *Materials Science and Engineering: A*, p. 483-484, 2008.
- [24] Q. Ma and D. Clarke, "Size dependent hardness of silver single crystals," *Journal of Materials Research*, vol. 10, no. 4, pp. 853-863, 1995.
- [25] M. Begley and J. Hutchinson, "The mechanics of size-dependent indentation," *Journal of the Mechanics and Physics of Solids*, vol. 46, no. 10, p. 2049-2068, 1998.

# Annex A: Experimental Apparatus

## A1: Tukon 1202 micro-hardness machine

Hardness Scales: Knoop and Vickers

Test Loads: 10, 25, 50, 100, 200, 300, 500, 1000 and 2000 gf

Dwell Time: 5 - 99 seconds

Test Cycle: Automatic (loading/dwell/unloading)

Standards Compliance: ASTM E384 & E92, EN-ISO 6507

Turret: 3 positions (1 indenter, 10x and 50x objectives)

Measuring Range: 200  $\mu\text{m}$  at 10x

Reference: Buehler, (2016), *Tukon 1202* [ONLINE]. Available at: <https://goo.gl/63Tr1f> [Accessed 18 May 2016].



## A2: DMTA RSA-G2 – 35N load cell

Force Range: 0.0005 N to 35 N

Force Resolution: 0.00001 N

Dynamic Displacement Range:  $\pm 0.00005$  to  $\pm 1.5$  mm

Displacement Resolution: 1 nm

Frequency Range:  $2 \times 10^{-5}$  to 100 Hz

Temperature Control Forced Convection Oven

Temperature Range: -150 to 600  $^{\circ}\text{C}^*$

Heating/Cooling Rate: 0.1-60  $^{\circ}\text{C}/\text{min}$ .

Reference: TA Instruments, (2014), *RSA-G2 DMTA* [ONLINE]. Available at: <http://goo.gl/AVE6Up> [Accessed 18 May 2016].



## A3: Instron 5969 – 10N & 100N load cells

Load measurement accuracy: 1/1000 of load cell capacity

Data acquisition rate: up to 2.5 kHz

Speed range: 0.001 - 3000 mm/min

Reference: ITW Test & Measurement, (2015), *5960 Dual Column Testing Systems* [ONLINE]. Available at: <http://goo.gl/33mBP9> [Accessed 18 May 2016]



#### A4: Imetrum non-contact video extensometer

Multi-point dynamic monitoring

Displacement measurement resolution: 0.3  $\mu\text{m}$

Data acquisition rate: up to 17 Hz



Reference: ITW Test & Measurement, (2015), *5960 Dual Column Testing Systems* [ONLINE].

Available at: <http://goo.gl/8cDbjc> [Accessed 18 May 2016]

#### A5. Cold rolling machine

Three different thickness settings were used: 2 mm, 1.10 mm, 0.80 mm, 0.3 mm, and 5 mm. Using two PTFA sheets, the smallest section was adapted to obtain 0.25mm indium sheets.



Reference: M&S, (2016), *T341187P Machine* [ONLINE].

Available at: <http://goo.gl/bey71r> [Accessed 18 May 2016].

#### A6: Zwick/Roell ZCP 020 cutting press

Principle: a manual cutting press using a bent lever.

The dogbone stencil standard: BS EN ISO 527-1:2012

Reference: Zwick/Roell, (2014), *ZCP 020* [ONLINE]. Available at:

<http://promarchive.com/product/151632> [Accessed 18 May 2016].



#### A7: Deben 200N Microtester Tensile/Compression

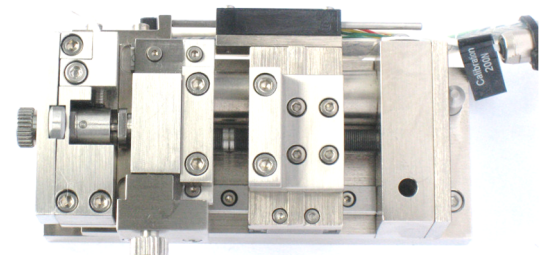
Exchangeable loadcell, accuracy readout +/-1%

Dynamic resolution 0.1%, static resolution 0.05% of full scale range

Standard speed range using 1119:1 gearbox: 0.1 mm/min to 1.5 mm/min

Distance between jaws: 10-20 mm

Reference: Deben UK Limited, (2016), *MICROTEST 200N* [ONLINE]. Available at: <http://goo.gl/rvDpxt> [Accessed 18 May 2016].



#### A8: LE-01 EIR Laser Extensometer

Measurement Range: 8-80 mm; Resolution  $\pm 0.005$  mm, Scan Rate: 100Hz

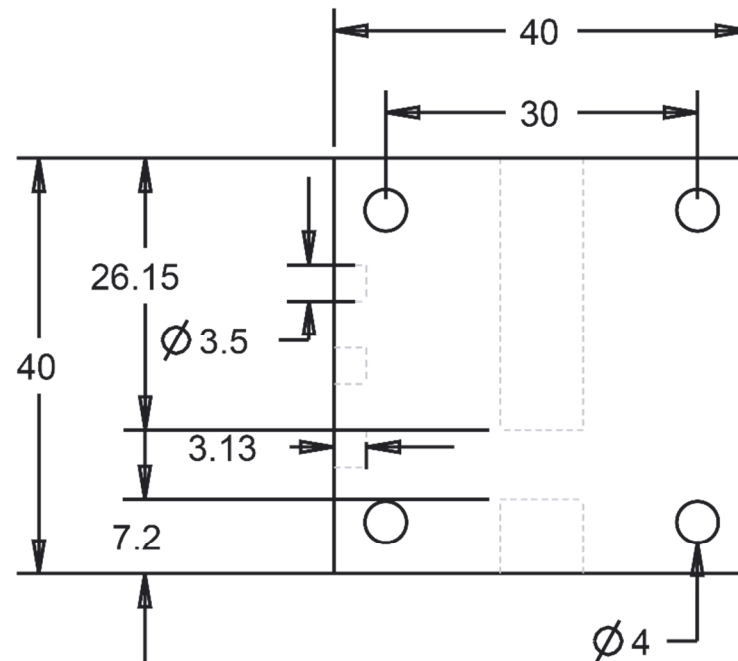
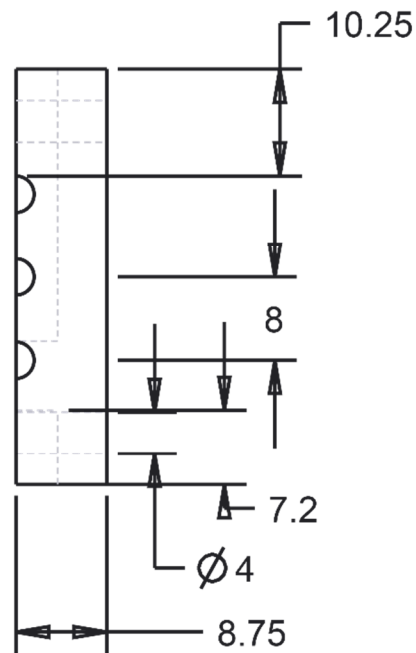
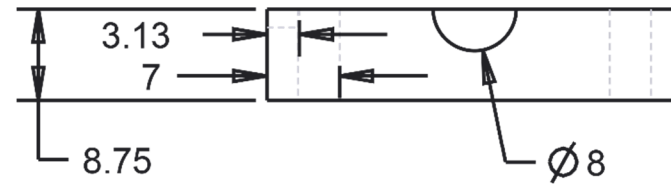
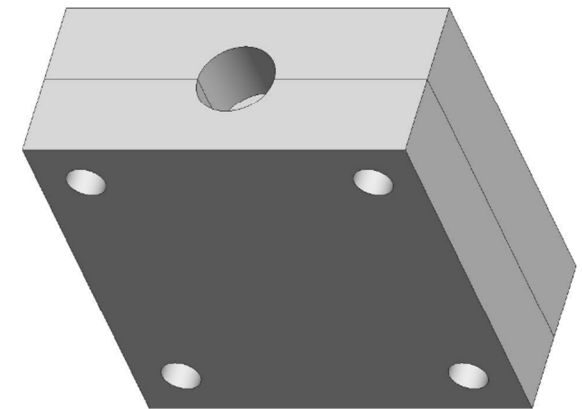
Target Distance: 250 mm nominal, 500 mm maximum, selectable

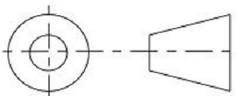
Reference: EIR (2012), *Laser Extensometers* [ONLINE]. Available at:

<http://e-i-r.com/> [Accessed 18 May 2016]

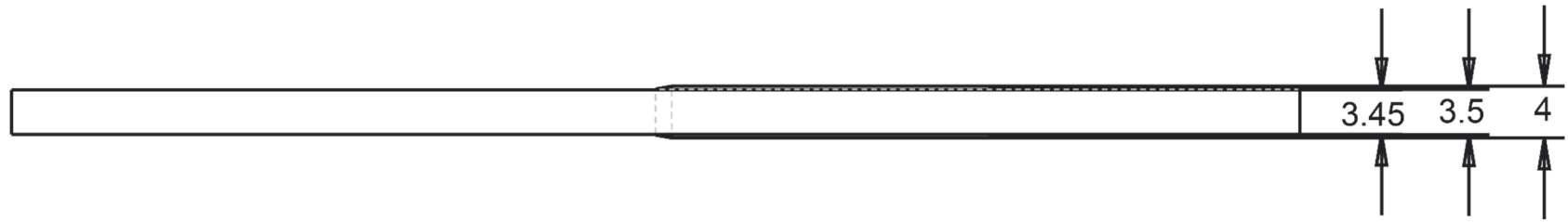
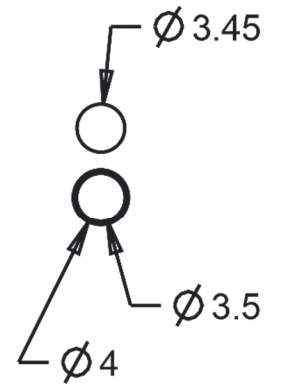
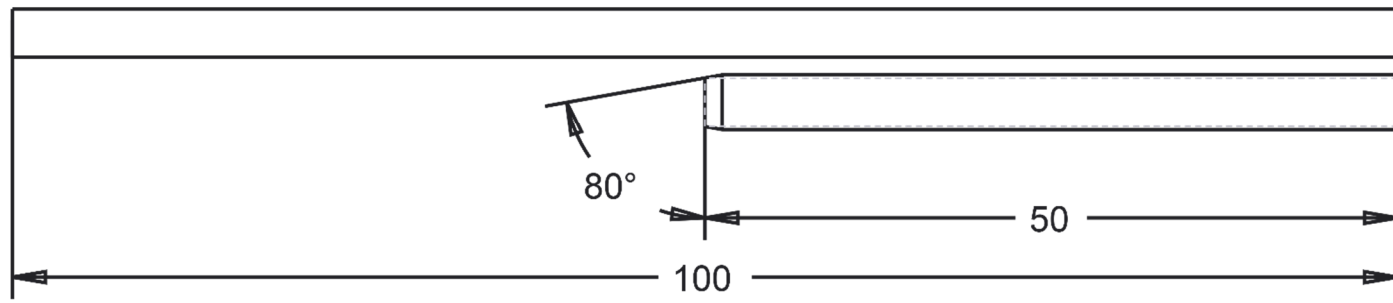
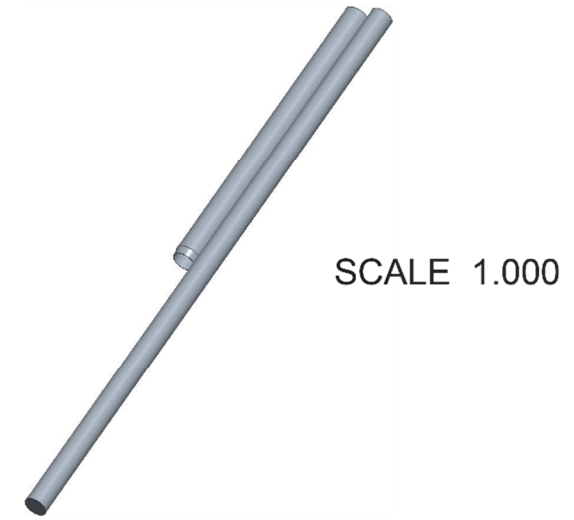


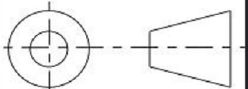
# Annex B1: Compression – Cylinder mould



	Author:	S.P. Iliev	Experiment:	Uniaxial Compression	Scale	All dimensions in mm	
	Supervisor:	V.L.Tagarielli	Part:	Specimen mould		1.5	
Indium FYP	Version 1.5	Date:12.02.16	Manufacturing:	CNC Machining/PMMA			

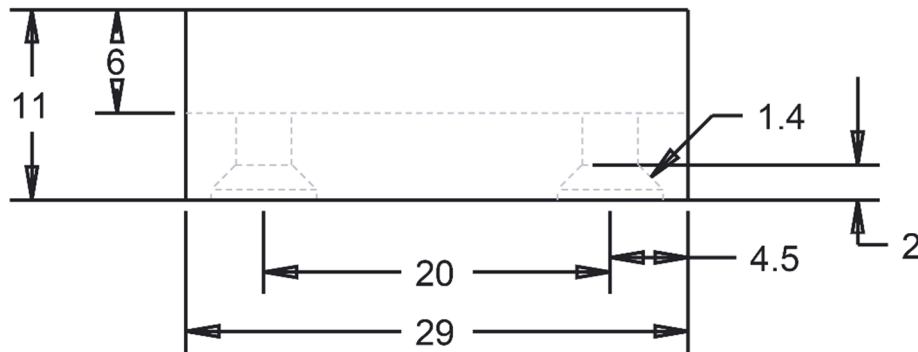
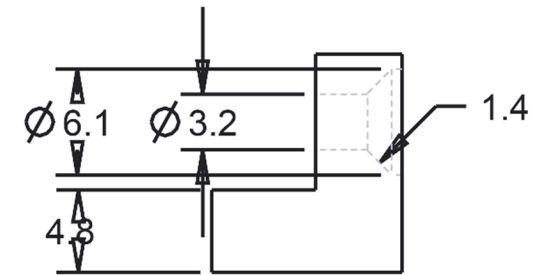
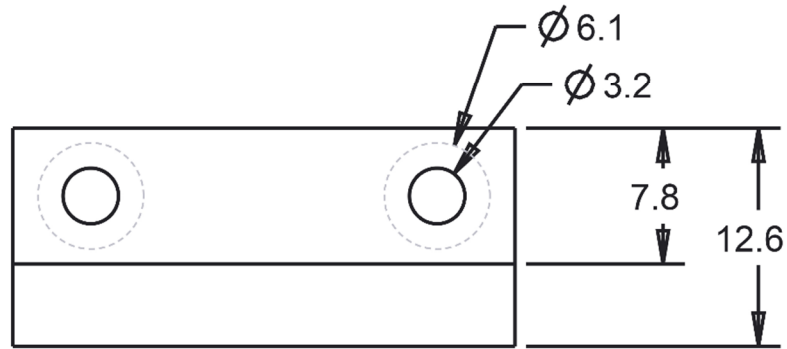
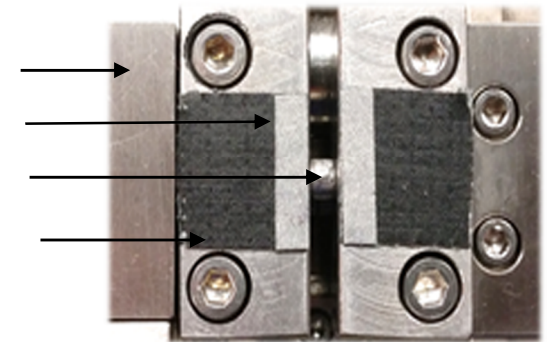
# Annex B2: Compression – Punch

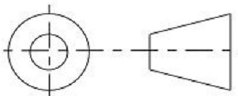


 Indium FYP	Author:	S.P. Iliev	Experiment:	Uniaxial Compression	Scale	All dimensions in mm	
	Supervisor:	V.L.Tagarielli	Part:	Custom punch	2		Tolerances
Version 1.0	Date:12.02.16	Manufacturing:	Milling/Al 6061	±0.02mm			

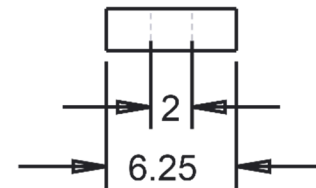
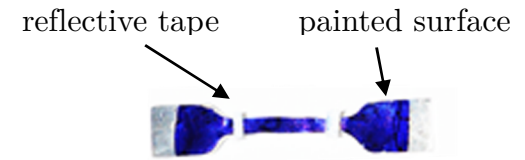
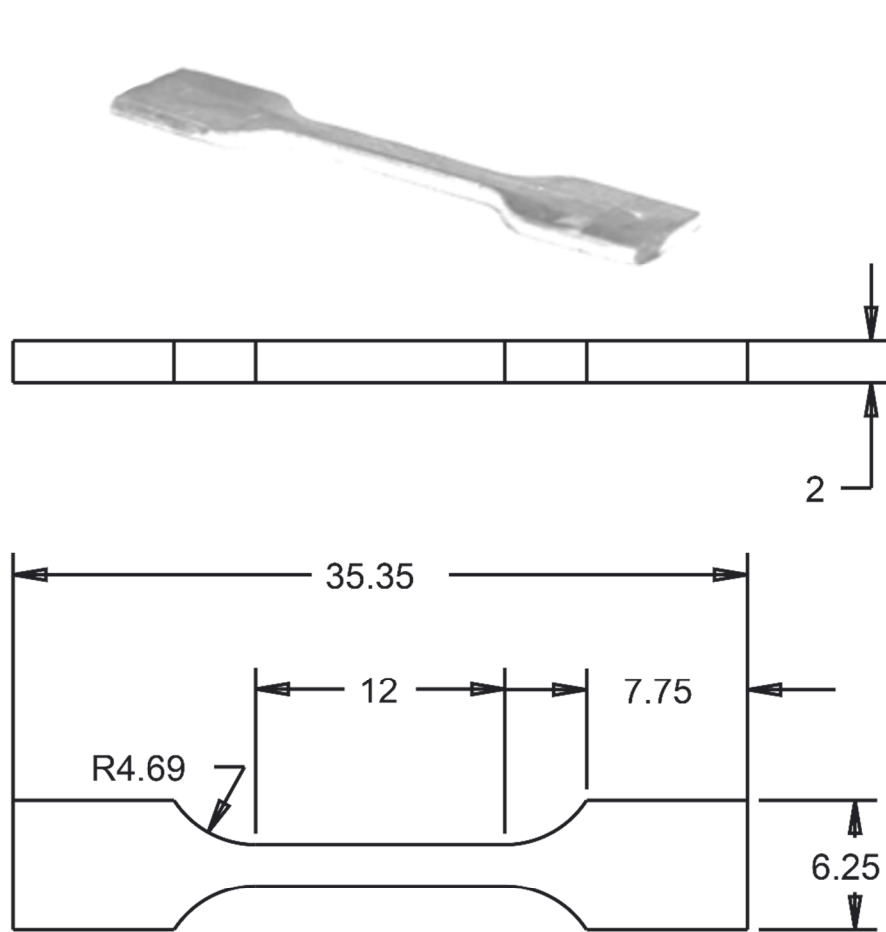
# Annex B3: Compression – Fixture

microtester  
 reflective tape  
 indium sample  
 masking tape

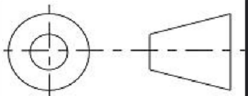


 Indium FYP	Author:	S.P. Iliev	Experiment:	Uniaxial Compression	Scale	All dimensions in mm	
	Supervisor:	V.L.Tagarielli	Part:	Microtester Fitting		2.5	
Version 1.0	Date:12.02.16	Manufacturing:	Milling/Steel				

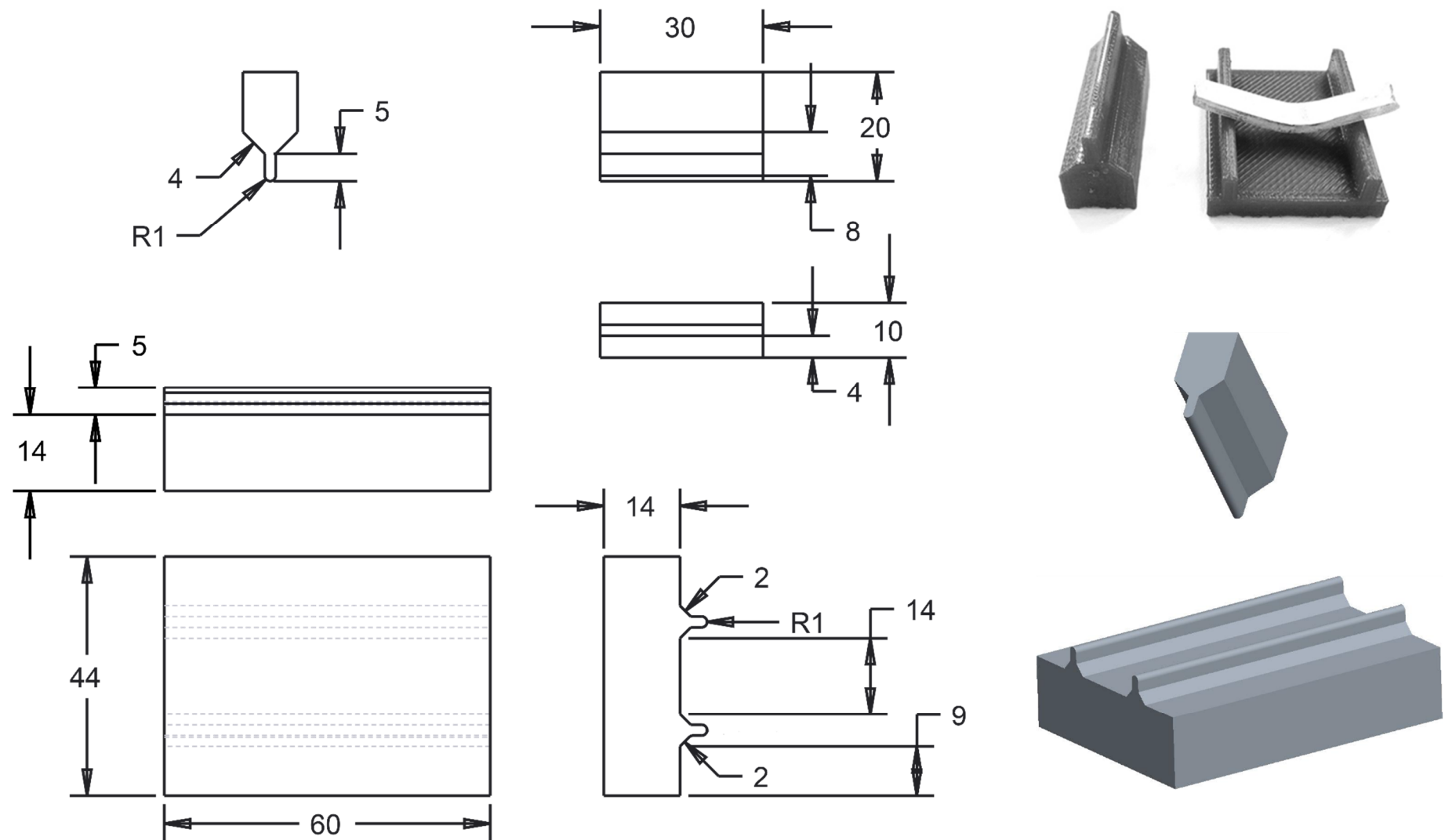
# Annex B4: Tension – Dogbone specimen

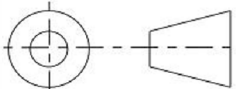


SCALE 1.000

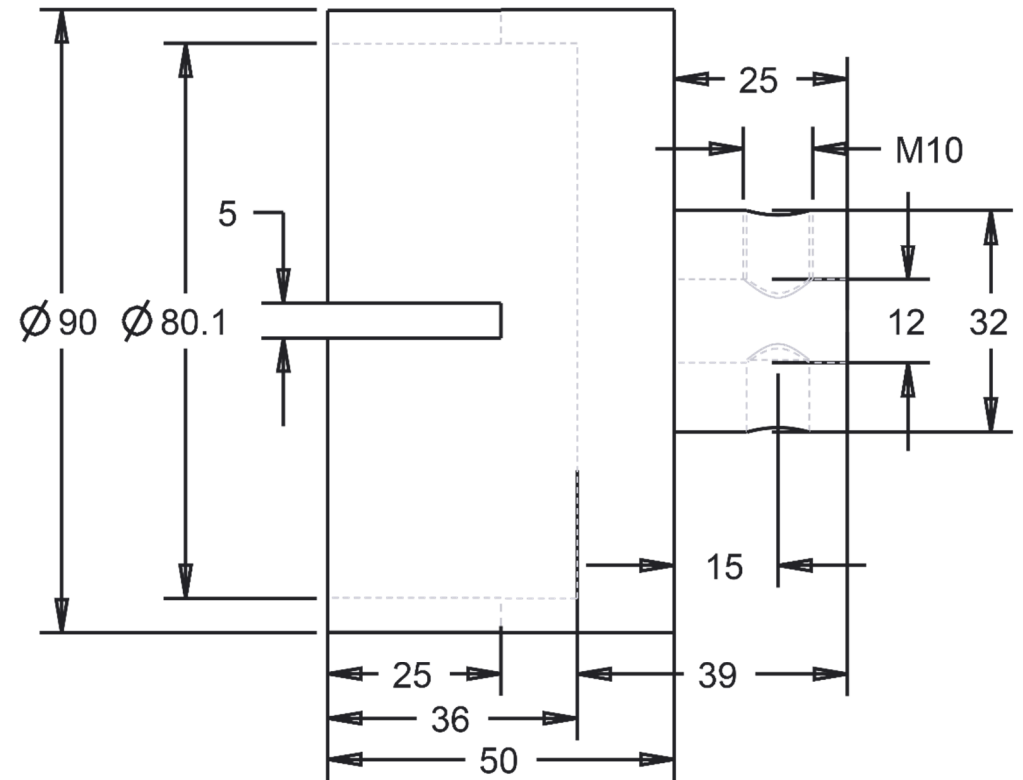
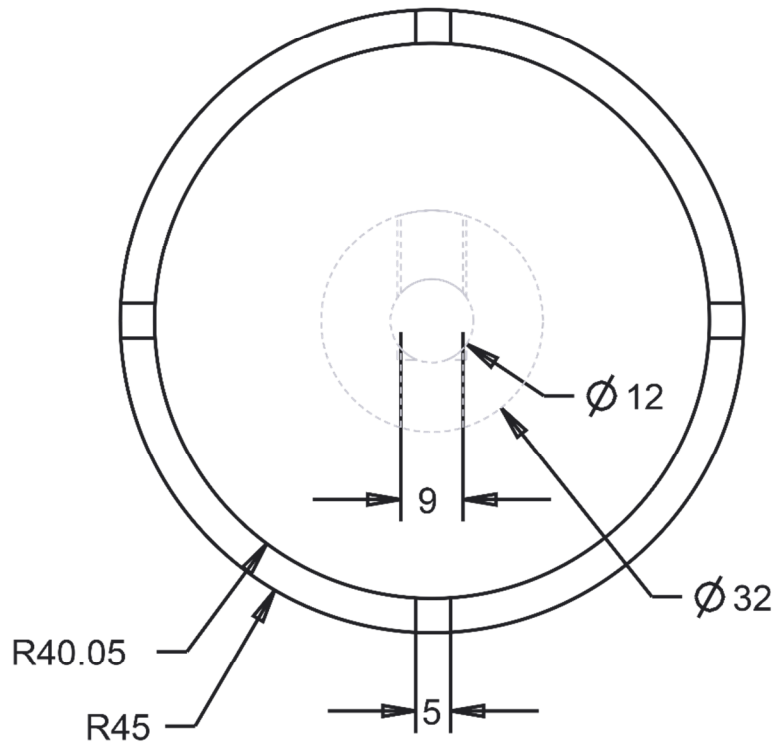
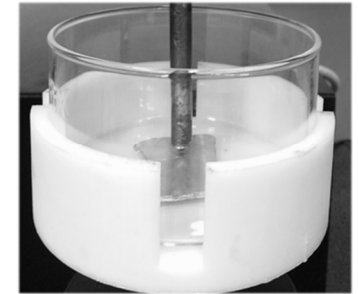
	Author:	S.P. Iliev	Experiment:	Uniaxial Tension	Scale	All dimensions in mm	
	Supervisor:	V.L.Tagarielli	Part:	Dogbone specimen		3	
Indium FYP	Version 1.0	Date:08.02.16	Manufacturing:	Punch Press/Indium			

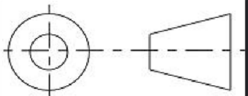
# Annex B5: Bending Fixture



	Author:	S.P. Iliev	Experiment:	3-point bending	Scale	All dimensions in mm	
	Supervisor:	V.L.Tagarielli	Part:	Test fittings		1	
Indium FYP	Version 1.0	Date:12.02.16	Manufacturing:	3D Printing/ABS			

# Annex B6: LN<sub>2</sub> Fixture

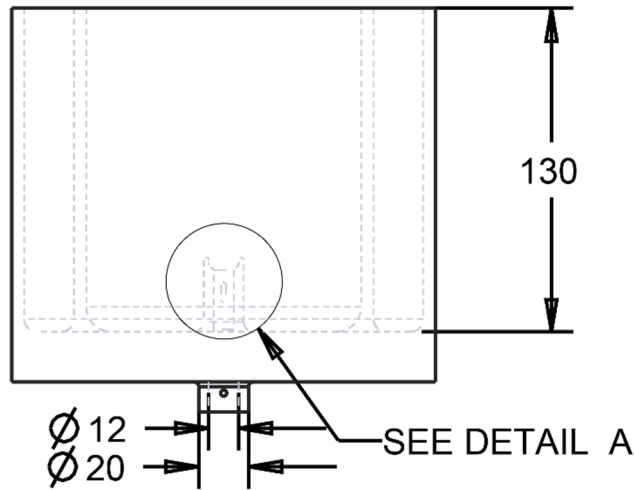
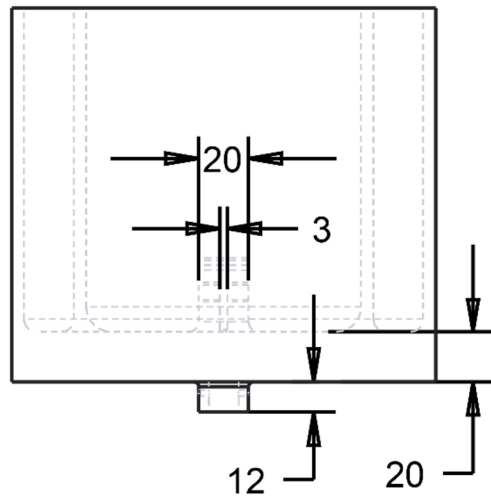
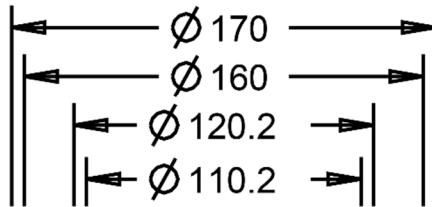
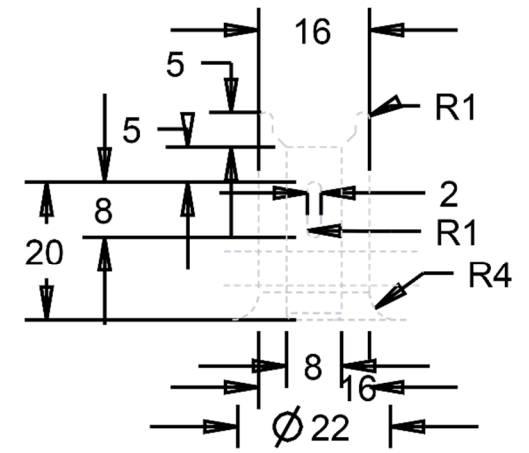
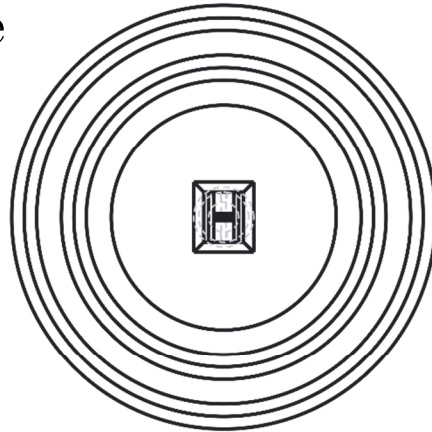


	Author:	S.P. Iliev	Experiment:	All. Cryogenic temp.	Scale	All dimensions in mm	
	Supervisor:	V.L.Tagarielli	Part:	LN2 Fixture	1		Tolerances
Version 1.0	Date:12.02.16	Manufacturing:	Connex 3 Printer/ABS	±0.1mm			

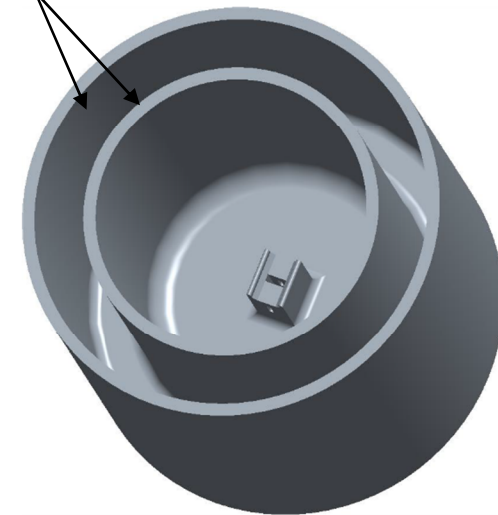
# Annex B7: LN<sub>2</sub> Fixture

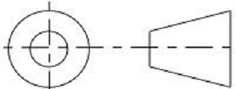
New Design

DETAIL A  
SCALE 1.000

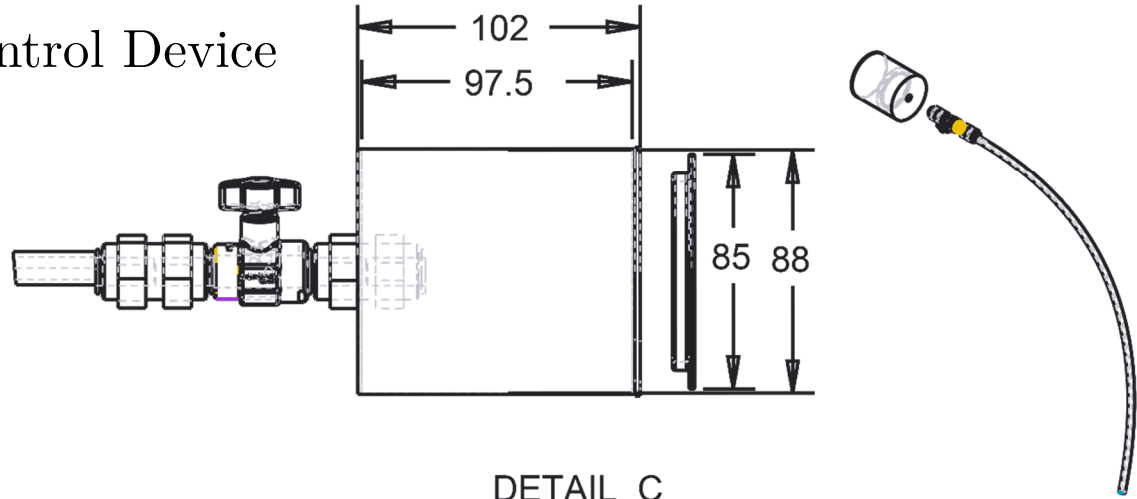


LN<sub>2</sub> chambers

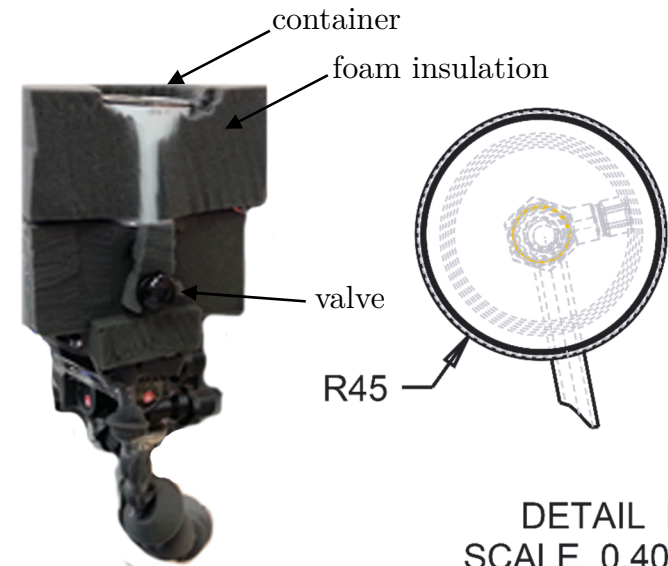
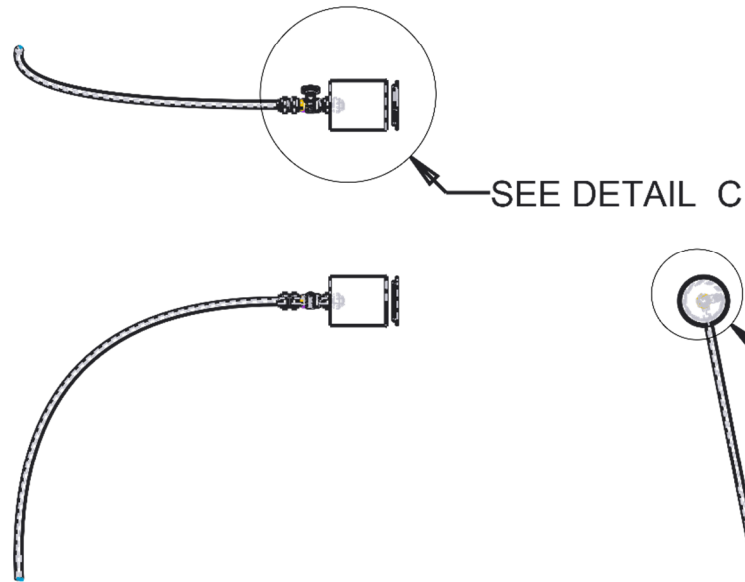


	Author:	S.P. Iliev	Experiment:	All. Cryogenic temp.	Scale	All dimensions in mm	
	Supervisor:	V.L.Tagarielli	Part:	LN2 New Fixture		0.36	
Indium FYP	Version 2.2	Date:28.01.16	Manufacturing:	Fortus 450 in ABS			

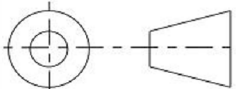
# Annex B8: LN<sub>2</sub> Debit Control Device



DETAIL C  
SCALE 0.400



DETAIL B  
SCALE 0.400

	Author:	S.P. Iliev	Experiment:	All. Cryogenic temp.	Scale	All dimensions in mm	
	Supervisor:	V.L.Tagarielli	Part:	LN2 Level Controller	0.8		Tolerances
Version 1.0	Date:12.02.16	Manufacturing:	Assmly of parts	±0.5mm			

# Annex C: Length scale model

There are two main theories to combining strain and its gradient by considering the individual contributions from SSD and GND: Fleck-Hutchinson (FH) and Nix-Gao (NG). These allow the determination of the length scale and yield strain from microbending or depth sensing data. The commonalities and differences of both theories are critically assessed by Evans and Hutchinson [5], yet the scope of this study shall be limited to their application to Indium.

## Annex C1: For microbending

The Fleck-Hutchinson model shall be used to evaluate the length scale  $l_{FH}$  and yield strain  $\varepsilon_{y,FH}$  from the microbending data. This model is based on plastic dissipation and is expressed as the sum of the SSD and GND contributions [5]:

$$E_P = [\varepsilon_P^\mu + (l_{FH}\varepsilon_P^*)^\mu]^{1/\mu} \quad (23)$$

Where  $\varepsilon_P$  is the plastic strain,  $l_{FH}$  is the length scale and  $\varepsilon_P^*$  is the magnitude of the gradient of plastic strain. The first term refers to plastic dissipation caused by the motion of the SSD, the second refers to GND contribution. Interactions between these components are neglected in the model (this is the case for the NG theory as well). Note that for small strain gradients this reduces to the classic Von Misses ( $J_2$ ) theory:  $E_P \cong \varepsilon_P$ .

The exponent  $\mu$  was initially set as 2 in the work carried out by Fleck and Hutchinson [11] due to mathematical considerations. However, Evans and Hutchinson [5, p. 1687] found that  $\mu = 1$  better matches experimental data. Hence this value shall be used.

Knowing that  $\nu = 0.4498$  [20, p. 1201], indium can be assumed a perfectly plastic solid. Considering an indium beam of thickness  $t$  and invoking the same approximations as Evans and Hutchinson [4, p. 1678] the FH model becomes:

$$\sigma \cong \sigma_{y,FH} \left(1 + l_{FH} \frac{2}{t}\right) \quad (24)$$

Where  $\sigma$  is the flow stress at a certain strain and  $\sigma_{y,FH}$  is the yield stress. It is now possible to determine  $l_{FH}$  and  $\sigma_{y,FH}$  from the experimental data. Finally, the yield strain is given by:

$$\varepsilon_{y,FH} = \frac{\sigma_{y,FH}}{E} \quad (25)$$

The Young Modulus of indium ( $E$ ) shall be considered 12.74 GPa [20].

## Annex C2: For indentation

The Nix-Gao model shall be used to find the length scale  $l_{NG}$  and yield strain  $\varepsilon_{y,NG}$  from the depth sensing indentation experimental data. The NG theory invokes an enhanced flow stress governed by the density of the GND [5], which can be expressed [9] as:

$$\rho_{GND} \cong \frac{\lambda}{V} = \frac{\pi h_P R / b}{2\pi R^3 / 3} = \frac{3}{2bh_P} \tan^2 \theta \quad (26)$$

where  $\lambda$  is the total length of the dislocation loops,  $V$  is the volume of the material in which the dislocations are distributed (assumed to be hemispherical),  $R$  is the indenter contact radius,  $\theta$  is the angle of the indented surface and  $h_P$  is the residual plastic depth. Knowing that  $\nu = 0.4498$  [20, p. 1201], it is safe to assume that  $h \cong h_P$  where  $h$  is the penetration depth. Since the Vickers indenter is self-similar,  $\theta$  is constant with respect to indentation depth and equal to  $68^\circ$ .

The Burgers vector  $b$  can be found to be  $229.81\text{E-}09$  mm since indium has a FCC crystal structure with known lattice parameters. The relationship between the density and shear strength is given by the Taylor hardening model [22] and this can be combined with the Misses flow rule  $\sigma = \tau\sqrt{3}$  to give the following relationship between flow stress and dislocation density:

$$\sigma = \alpha\mu b\sqrt{\bar{r}\rho_{GND} + \rho_{SSD}}\sqrt{3} \quad (27)$$

Where  $\mu$  is the shear modulus. Substituting (26) into (27) and rearranging gives:

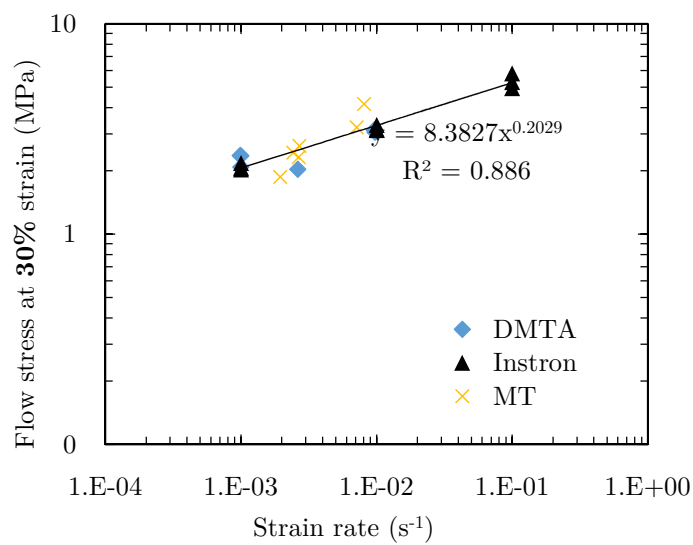
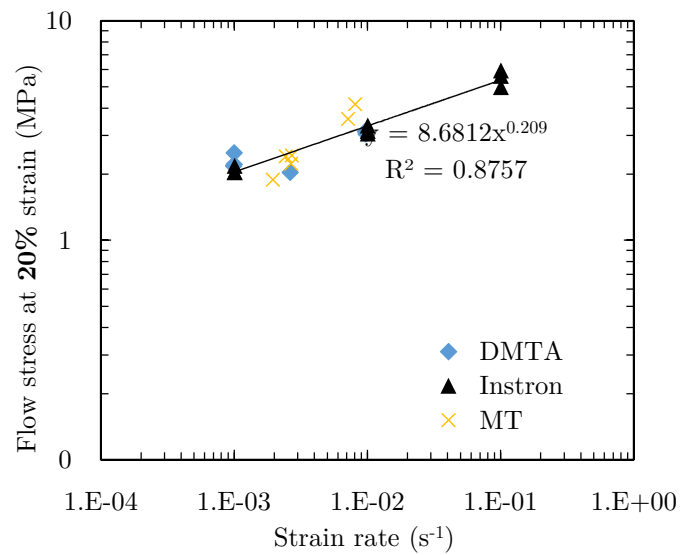
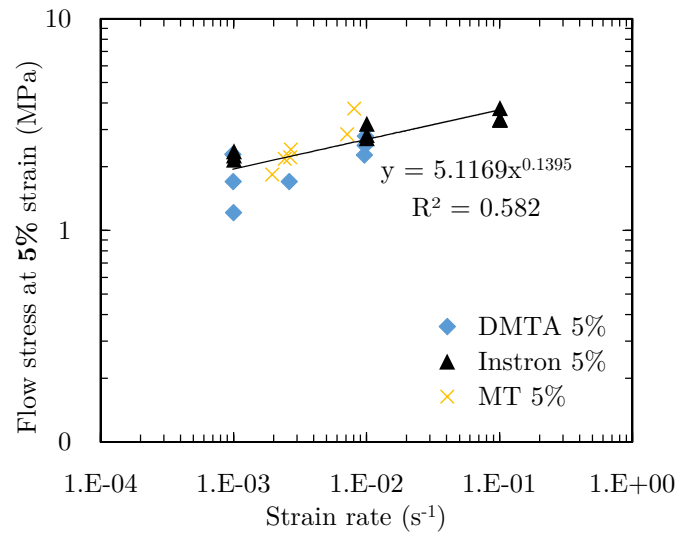
$$\sigma \cong \sqrt{3}\alpha\mu b\sqrt{\rho_{SSD}}\sqrt{1 + \frac{\bar{r}3 \tan^2 \theta}{2b\rho_{SSD}} \frac{1}{h}} \quad (28)$$

It is now possible to represent  $\sigma_{y,NG} = \sqrt{3}\alpha\mu b\sqrt{\rho_{SSD}}$  as the macroscopic yield stress as well as  $h^* = \bar{r}3 \tan^2 \theta / 2b\rho_{SSD}$  as a length scale associated with the depth dependence of hardness for spherical indenters. The latter can be adapted for a Vickers indenter by using the correlation factor developed by Swadener *et al.* [9], thus  $l_{NG} = h^*/5.2$ . Finally, the stress can be related to the hardness by using the Tabor factor [19], to give:

$$H \cong H_0\sqrt{1 + \frac{l_{NG}}{5.2h}} \quad (29)$$

It is now possible to fit this model to the experimental data and obtain the values of interest.

# Annex D: Strain rate effects in compression



Strain rate sensitivity shown through a log-log plot of flow stress vs strain rate of 5% in the hardening phase (top), as well as at 20% (mid) and 30% strain (low) in the saturation phase. Experiments were carried out with the Instron, DMTA and MT machines. The power law fits to the data give the parameters presented in Table 1.